Journal of Materials Chemistry A

ROYAL SOCIETY OF CHEMISTRY

REVIEW

View Article Online
View Journal | View Issue

Cite this: J. Mater. Chem. A, 2022, 10, 5813

Mechanistic understanding and design of non-noble metal-based single-atom catalysts supported on two-dimensional materials for CO_2 electroreduction

Ya Huang, [a] Faisal Rehman, [a] Mohsen Tamtaji,[a] Xuning Li,[b] Yanqiang Huang, [b] Tao Zhang*[b] and Zhengtang Luo *[a]

Single-atom catalysts (SACs), which are low-cost, contain earth-abundant metals, and feature two-dimensional material supports, have shown great potential for us in a wide range of electrochemical reactions, including the CO_2 reduction reaction (CO_2RR) to convert CO_2 to valuable chemicals and fuels. In recent years, substantial advances have been achieved in the preparation methodologies, with improved catalytic performances, but the underlying structure–activity relationship from a general perspective remains elusive. In particular, it is urgent to summarize the progress made on SACs with diatom metal centers toward efficient CO_2RR. Based on the recent progress in this area, this review synopsizes the fundamental understandings of non-noble metal-based SACs for CO_2RR using selected examples. We also highlight the representative atomic structures of active sites from the latest progress, including M–N–C, heteroatom co-doping, vacancy/edge defects and bimetallic SACs, with the aim of elucidating the nature of active sites on various 2D substrates. Moreover, we summarize the spectroscopic and computational studies to verify the atomic-level regulation of the geometric and electronic properties of SACs. We anticipate that this review will deepen the mechanistic understanding of the structure–performance relationship and inspire future studies on SACs for CO_2RR.

Received 27th September 2021
Accepted 25th November 2021

DOI: 10.1039/d1ta08337f

rsc.li/materials-a

1. Introduction

The environmental issues brought about by the tremendous consumption of fossil fuels has led to the exploration of renewable energy.[1–3] According to a recent report, the global average concentration of CO_2 in the atmosphere reached a recorded level of over 415 ppm in the first half of 2021 and this trend is expected to continue in the next 20 years if no counteraction is taken.[4] The urgent need for clean energy technologies in reducing atmospheric CO_2 concentration presents a great research challenge and opportunity.[5] In recent decades, tremendous efforts have been made in the field of electrochemical CO_2 reduction reaction (CO_2RR), to mitigate global warming and tackle the worldwide energy shortage.[6–9] Ultimately, carbon neutrality can be achieved by converting CO_2 into storable valuable fuels, such as methane, methanol, formate, ethanol, *etc.*[10,11] Since the implementation of the CO_2RR mainly relies on high-performance electrocatalysts, the development of highly efficient and scalable catalysts is the key. Significant insights have been obtained from extensive studies on bulk or nanoscale electrocatalysts over the past few years.[12,13] However, two issues are notably worthy of being considered for these categories: (1) low atomic utilization, where only a small fraction of metal atoms are electrochemically active during electrolysis, and (2) relatively poor selectivity due to the high kinetic barriers of CO_2 activation and the competing hydrogen evolution reaction (HER).[14–16] The emerging single-atom catalysts (SACs), with adjustable geometric and electronic structures of their catalytic sites, have been considered as ideal candidate to address this dilemma.

SACs are catalysts with atomically isolated metal active sites stabilized by a support, which were first introduced by Zhang, Li, Liu, and co-workers in 2011.[17] This work put forward the first example of Pt SACs dispersed on FeO_x for CO oxidation and demonstrated the catalytic mechanism through density functional theory (DFT) studies. After this, SACs as a new class of heterogeneous catalysts rose to be a research hotspot, with substantial work being carried out. The interest in SACs towards the CO_2RR arises from three main aspects: (1) their extremely high atom efficiency, where every single atom is exposed as

[a]Department of Chemical and Biological Engineering, Guangdong-Hong Kong-Macao Joint Laboratory for Intelligent Micro-Nano Optoelectronic Technology, William Mong Institute of Nano Science and Technology, Hong Kong Branch of Chinese National Engineering Research Center for Tissue Restoration and Reconstruction, The Hong Kong University of Science and Technology, Clear Water Bay, Kowloon, Hong Kong, 999077, P. R. China. E-mail: keztluo@ust.hk

[b]State Key Laboratory of Catalysis, Dalian Institute of Chemical Physics, Chinese Academy of Sciences, Dalian 116023, Liaoning, China. E-mail: taozhang@dicp.ac.cn

a reactive site.[18] (2) The low coordination state of the metal single atom directly affects the electronic and geometric properties and therefore leads to different catalytic activities.[19–21] Compared with non-SACs, atomically dispersed 3d nonprecious metals (especially Fe, Co, and Ni) exhibit better selectivity towards CO_2RR over the HER.[22–24] (3) SAC coordination into a graphitic framework can be easily simulated using DFT calculation models. Such simplicity of active regions endows them to be ideal platforms to study catalytic mechanism.[25]

Research on CO_2 electro-conversion has made a significant breakthrough recently and has been categorized according to various factors. For instance, a series of SAC fabrication methods, substrate materials, the types of central metals, and the preferred products have been systematically summarized in previous reviews.[26–30] Despite numerous progress reports on SACs for electrochemical reactions, the catalytic design strategies and experimental performance have been substantially focused upon, while the additional insights into the spectroscopies and underlying relationship among different atomic structures for the CO_2RR have been rarely systematically reviewed. To narrow the scope, this review discusses nonprecious metal-based SACs, especially those featuring 3d transition metals. Non-noble metal single atoms have been widely studied as carbon-based low-cost SACs show great possibility to replace the noble metal versions and be scaled up to an industrial level in the future.[28,31,32] Among them, Cu has been found to be a unique metal that can reduce CO_2 to C_2 or C_{2+} products, which plays a decisive role in this field and requires more attention.[11,33–35]

As shown in the workflow chart (Fig. 1), this review begins with fundamental knowledge on the CO_2RR selected from recent representative works and factors that can impact the selectivity of SACs. In-depth insights into a variety of molecular models with diverse coordination structures extracted from carbon-based SACs, involving M–N–C systems, heteroatom co-doping, vacancy/edge defects and bimetallic models are discussed. Special attention is paid to the recent development of advanced spectroscopies that can be used to identify the atomic structures of SACs and interpret their evolution during electrolysis. Furthermore, we present a computational part, which focuses on DFT and machine learning (ML), providing atomic-level insight into SACs and reaction mechanisms. Finally, major challenges and perspectives on non-noble metal-based SACs are discussed. We hope this review can pave the way towards the rational design of SACs and provide fundamental guidance for the future research on the CO_2RR. The abbreviations using it in the review are listed in the Table 1.

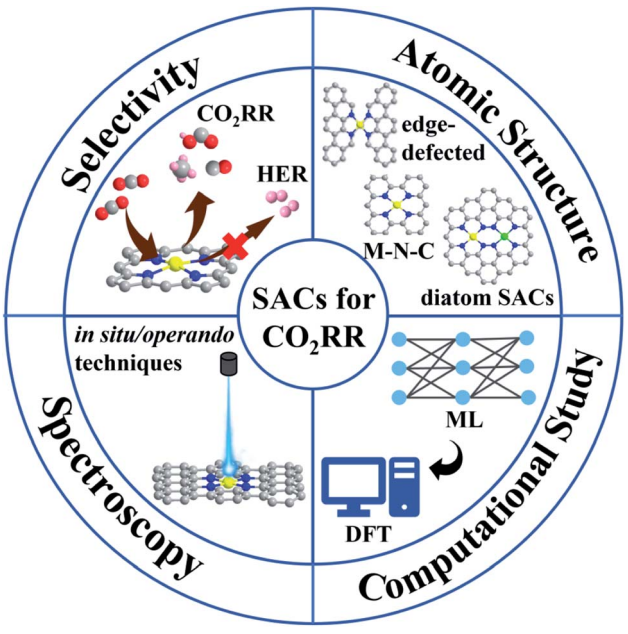

Fig. 1 Workflow chart of this review. The review follows four steps, including the selectivity of SACs, atomic structural tuning, advanced spectroscopy, and computational study.

2. Fundamentals of the CO_2RR on SACs

The mechanism pathways of the CO_2RR are complex due to multi-electron transfer leading to various possible products.[14] This process starts with CO_2 adsorption on the active sites, followed by the step-wise transfer of protons (H^+) and/or electrons (e^-) and generation of diverse intermediates and products.[36] As illustrated in Scheme 1a, the CO_2 molecule is first activated to *COOH *via* a one proton-coupled electron transfer (PCET) process.[37] This step is critical for the determination of the selectivity of SACs due to the existing competition of *H adsorption. It should be noted that the species illustrated in Scheme 1 represent the product formation based on the number of electrons/protons transferred. Two-electron transfer is commonly observed for SACs, with CO or HCOOH being released as final products. And deeply reduced C_1 products like methanol and methane require six and eight H^+/e^- transfer, respectively. Scheme 1b illustrates the proposed pathways toward C_2 products, where the OC–CO dimerization is the rate-determining step (RDS).[37] An alternative pathway toward C_2 products is through the coupling of *CHO/*COH and *CO, which has been theoretically proved on diatom SACs supported by 2D graphene nitrene.[38] All subsequent evolutions of species come from these C–C coupling processes. Notably, stabilized C_2 intermediates can be transferred to *n*-propanol *via* CO insertion,[34] but it is very difficult for this to take place on SACs, therefore this pathway will not be discussed in detail in this review.

In contrast to bulk and nanostructured non-noble metals, which have been developed on an industrial-scale and exhibit high current densities toward C_2 products, the majority of SACs for the CO_2RR are still at the stage of laboratory studies.[39,40] The most commonly used H-type electrolyzer for the CO_2RR, constructed from two gas-tight half-cell chambers separated by an ion-exchange membrane, is illustrated in Fig. 2a. Furthermore, the half-cell reactions in the CO_2RR with their reduction potentials of the main products at pH 7 are listed in Table 2.[41] Most commonly, the CO_2RR on SACs proceeds through a two-electron transfer process and generates CO or formate, balanced with oxygen evolution reaction (OER) as the anodic

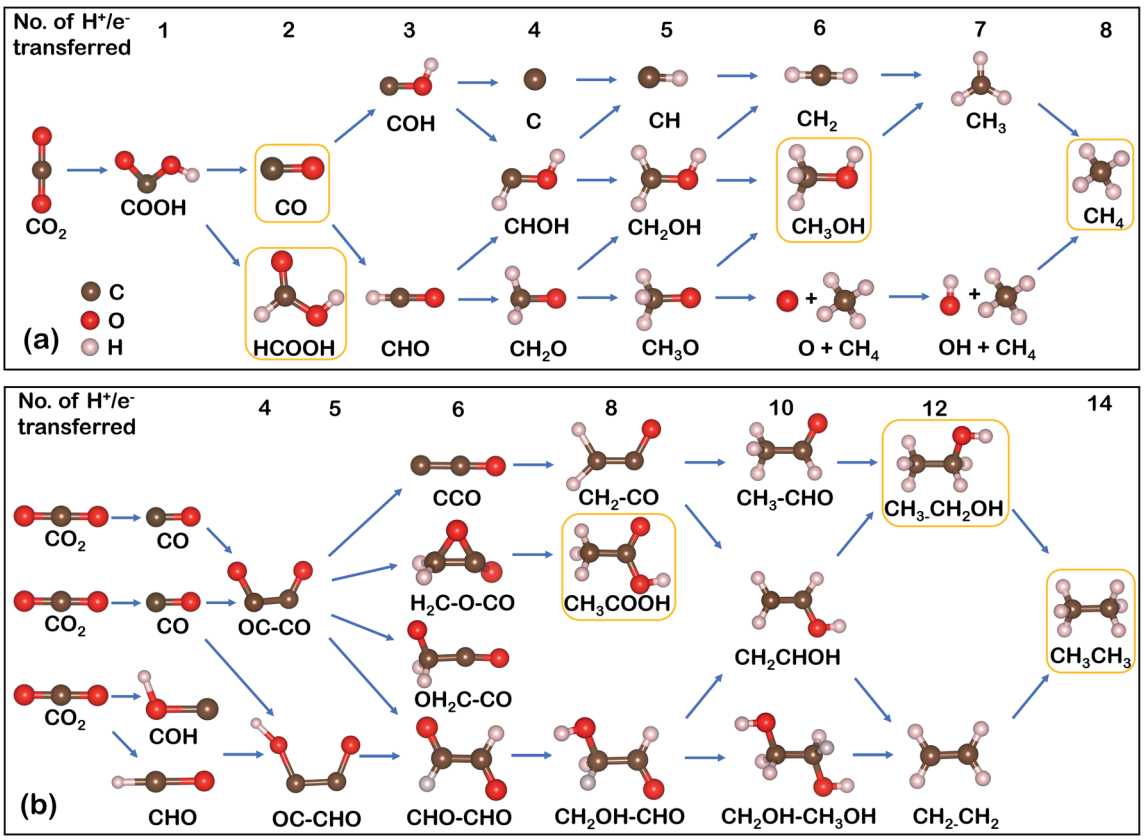

Scheme 1 Overview of possible CO_2RR roadmaps. The product formation of CO_2RR on SACs toward various (a) C_1 and (b) C_2 products (main products are boxed) with the number of H^+/e^- transferred.

reaction.[10] However, the selectivity of the CO_2RR over carbon-based SACs requires specific attention because several factors are believed to influence the catalytic performance and reduced products. In this section, selected fundamental factors and how they impact CO_2 activation and intermediate stabilization will be discussed.

2.1 Metal center selection

A big challenge associated with the CO_2RR is the competitive HER in aqueous electrolytes. From a thermodynamic perspective, the reduction potential from CO_2 to CO is slightly different from the HER ($E^0(CO_2/CO) = -0.11$ V *vs.* RHE).[41] However, the

Table 1 A table of abbreviations in this review

1E_M	First ionization energy	MOFs	Metal–organic frameworks
ATR-IR	Attenuated total reflection-infrared	MS	Intermedium-spin
C_2N	Nitrogen-doped graphene	OCV	Open-circuit voltage
CO_2RR	CO_2 reduction reaction	OER	Oxygen evolution reaction
COFs	Covalent organic frameworks	Pc	Phthalocyanine
DFT	Density functional theory	PCET	Proton-coupled electron transfer
DOS	Density of state	RDS	Rate-determining step
E_M	Pauling-electronegativity	RHE	Reversible hydrogen electrode
EXAFS	Extended X-ray absorption fine structure	SACs	Single-atom catalysts
FE	Faradaic efficiency	TCNQ	Tetracyanoquinodimethane
FT	Fourier transform	TM	3d transition metal
g-C_3N_4	Graphitic carbon nitride	TOF	Turnover frequency
GQDs	Graphene quantum dots	TPP	Porphyrin
HER	Hydrogen evolution reaction	WT	Wavelet transform
HS	High-spin	XANES	X-ray absorption near-edge structure
j_{CO}	CO partial current density	XAS	X-ray absorption spectroscopy
LS	Low-spin	XGBR	Extreme gradient boosting regression
M_cov	Covalent radius	ΔG	Gibbs free energy
MEA	Membrane electrode assembly	η	Overpotentials
ML	Machine learning		

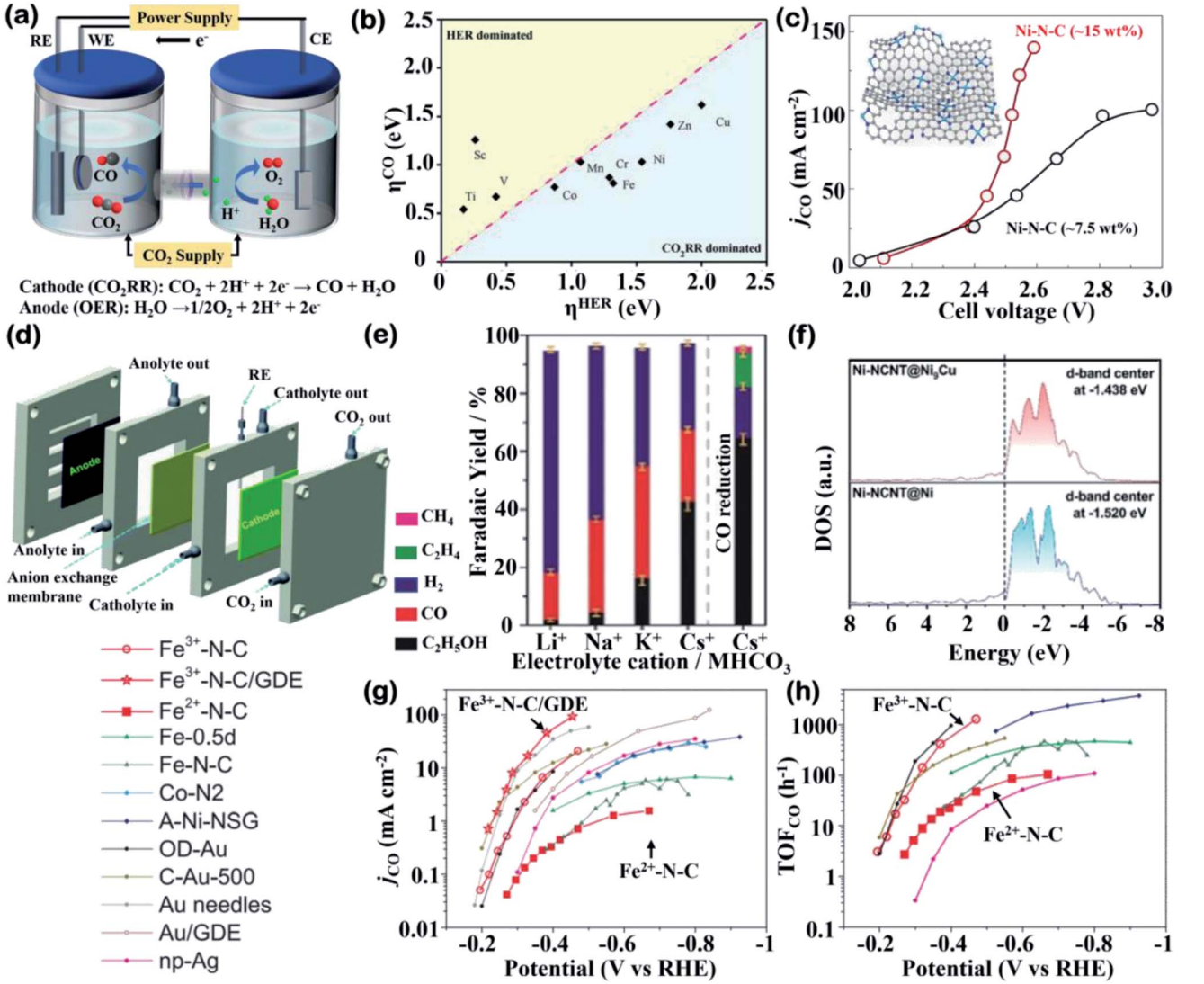

Fig. 2 Cell configurations and electrochemical data. (a) A CO_2 reduction H-cell with electrode reaction toward CO. (b) Overpotential for CO_2RR against that for HER on 3d transition metal SACs. Reproduced with permission from ref. 19, copyright 2021, Wiley-VCH. (c) The partial current densities of CO (j_{CO}) of nearly 7.5 wt% and 15 wt% Ni–N–C catalysts under different cell voltages. Inset: illustration of SACs prepared with the crosslinking and then self-assembled GQDs. Reproduced with permission from ref. 62, copyright 2019, Springer Nature Publication. (d) Schematic illustration of the flow cell configuration for CO_2RR. Reproduced with permission from ref. 65, copyright 2021, Royal Society of Chemistry. (e) faradaic yields (FY) of CO_2RR at −1.2 V *vs.* RHE in 0.1 M various cationic (Li^+, Na^+, K^+ and Cs^+) electrolytes. FY of CO reduction at −1.2 V *vs.* RHE in 0.1 M $CsHCO_3$ was reported on the right-hand side. Reproduced with permission from ref. 69, copyright 2019, Wiley-VCH. (f) Calculated DOS for Ni d-band center in Ni-NCNT@Ni and Ni-NCNT@Ni_9Cu. Reproduced with permission from ref. 76, copyright 2020, Wiley-VCH. (g and h) Comparison of (g) j_{CO} and (h) TOF toward CO of Fe^{3+}–N–C in an H-cell (red circles) and on a GDE (red stars) and of Fe^{2+}–N–C (red squares) as well as other reported catalysts. Reproduced with permission from ref. 77, copyright 2019, Science.

high kinetic barrier of CO_2 activation leads to a sluggish reaction rate, which requires careful selection of metal centers and improved catalyst designs.[42] Due to the reduction process mainly occurring at metal sites, the type of the metal center directly leads to distinct electronic properties and further affects the reaction pathways. By using density functional theory (DFT) calculations, SACs embedded in porphyrin-like supports with M–N_4–C active sites have been extensively investigated to predict efficient non-noble metals for the CO_2RR.[43,44] DFT calculations have revealed that the overpotentials (η) for the CO_2RR and HER at the atomic 3d transition metal (TM) sites and it has been found that the CO_2RR is favorable over the HER on most SACs (Fig. 2b). A new descriptor has also been established associated with the charge state of metal atoms to reassess the CO_2RR activity to exclude the HER influence, which provides rational guidance towards metal center selection.[19] The distinct catalytic performance of SACs compared to metal nanocrystals may be attributed to isolated M–N–C sites suppressing the *H adsorption and therefore alleviating the HER competition.[44,45] For example, an investigation among various M–N–C catalysts demonstrated that Fe and Co exhibit the best catalytic efficiency at low and high potentials, respectively,

Table 2 Thermodynamic reactions of the main products from the CO_2RR and their reduction potentials [*vs.* RHE] at pH 7. Reproduced from ref. 41, copyright 2021, Wiley-VCH

Product	Half-cell reaction	E^0 (V *vs.* RHE)
Hydrogen	$2H^+ + 2e^- \rightarrow H_2$	0
Carbon monoxide	$CO_2 + 2H^+ + 2e^- \rightarrow CO + H_2O$	−0.11
Formate/formic acid	$CO_2 + 2H^+ + 2e^- \rightarrow HCOOH$	−0.21
Methanol	$CO_2 + 6H^+ + 6e^- \rightarrow CH_3OH + H_2O$	0.03
Methane	$CO_2 + 8H^+ + 8e^- \rightarrow CH_4 + 2H_2O$	0.17
Acetate/acetic acid	$2CO_2 + 8H^+ + 8e^- \rightarrow CH_3COOH + 2H_2O$	−0.26
Ethylene	$2CO_2 + 12H^+ + 12e^- \rightarrow C_2H_4 + 4H_2O$	0.07
Ethanol	$2CO_2 + 12H^+ + 12e^- \rightarrow CH_3CH_2OH + 3H_2O$	0.09

consistent with the experimental observation that the CO_2RR activities of Fe and Ni SACs could rival those of noble metal-based (Ag or Au) catalysts.[46] It can be explained by the changes in the Gibbs free energies at the RDS that Fe and Co–M–C catalysts are both favored in the first PCET step under low overpotentials, but Co suffers from a high energy barrier in CO formation. On the other hand, Ni-based catalysts with weak binding of COOH* required large overpotentials and their weak *H adsorption under a large potential suppresses the HER.[46] Similar results from another study proved a volcano relationship between the CO_2RR performance and a family of M–N–C catalysts, and demonstrated that Fe and Co SACs are located at the summit of the volcano under different overpotentials.[47]

2.2 Loading and distribution

Despite the metal center being used to guide DFT calculations, the loading and distribution of SACs play a key role in enhancing selectivity and deeper reducing of CO_2 toward C_2 products. Due to the high surface energy of isolated metal atoms, substrates such as carbon-based supports, metal alloys or metal oxides are essential to stabilize single atoms and prevent their aggregation.[18,42,48–50] Low single-atom densities (typically less than 5 wt%) hamper electrocatalytic rates and catalyst usage for the CO_2RR. Therefore, huge efforts have been devoted to the design and synthesis of supports for higher loading of SACs.

The commonly used strategies include metal ion/molecule-seeding pyrolysis,[51,52] polymer-assisted pyrolysis,[53] metal–organic framework (MOF)-derived pyrolysis,[54,55] and covalent organic frameworks (COF)-supported methods.[56,57] The seeding strategy, polymer-assisted pyrolysis, and MOF-derived pyrolysis are widely applied due to their universal and facile operation for most metals, as summarized in many previous reviews.[41,45,49,58,59] On the other hand, the recent emerging pyrolysis-free COF-supported SACs are prepared *via* a mild and well-defined synthetic method with better control of the structure of the active sites. Covalently constructed using diverse organic modules, COFs act as a versatile platform for stabilizing single metal atoms with single distribution. Besides this, the N-containing organic building blocks in COF structures are CO_2-philic and can facilitate CO_2 adsorption during electrocatalysis, while the S-containing aromatic heterocycles are electron-rich and can serve as electron donors.[57,59,60] For instance, stable metal–porphyrin–tetrathiafulvalene COFs (M-TTCOFs) have been developed for the CO_2RR and a faradaic efficiency (FE) of 91.3% was achieved for CO at −0.7 V *vs.* RHE, as well as high cycling stability for over 40 h. Exfoliated COFs have a high number of active sites, which hence boost the FE to almost 100% at −0.8 V *vs.* RHE. This high efficiency may be ascribed to the synergistic combination of electron-migrating porphyrinic ligands and electron-donating tetrathiafulvalene.[56] This donor–acceptor conjugation is a promising approach by which to design polycrystalline COFs that exhibit a high electron transfer rate. Another strategy involves the incorporation of S-containing aromatic heterocycles with porphyrinic electron acceptors to prepare COF-supported Co-SACs. The catalysts exhibit outstanding electron conduction (1.38×10^{-8} S m^{-1}) and carrier mobility (0.18 cm^2 V^{-1} s^{-1}) and a FE_{CO} of 91.4% was achieved at −0.6 V *vs.* RHE.[61] However, the biggest challenges for COF-supported SACs are their relatively high cost and complicated preparation processes.

In recent work, low-cost ultrahigh loading SACs were synthesized *via* a facile route, in which amine-functionalized graphene quantum dots (GQDs) were used as a support on which to anchor metal atoms, achieving a record high content at 40 wt% or 3.8 at%. Using the general synthetic protocol, these mass-produced GQDs could be interwoven into a carbon matrix and applied in a flow cell reactor, featuring an anion membrane electrode assembly (MEA) with a Ni-SAC. The CO_2RR results (Fig. 2c) demonstrated that ∼15 wt% Ni-SACs reached the highest CO partial current densities, representing a 2.5-fold improvement over ∼7.5 wt% counterparts at a lower applied voltage of 2.55 V.[62] This example clearly shows that high loading is a prerequisite for the development of SACs toward their future industrialization.

2.3 Electrolyzer and electrolyte

The poor solubility of CO_2 (*ca.* 34 mM) in aqueous electrolytes leads to CO_2 diffusion limitations in H-type cells, which may not affect the catalytic performance at a moderate overpotential but hinder the development of high-loading SACs at a relatively high overpotential.[63,64] To enhance the kinetics of the CO_2RR, a flow cell can operate as a promising electrolyzer. In a very recent study, an amino-modification strategy was used to facilitate the current density of M–N–C (M = Ni, Fe and Zn) SACs for the CO_2RR. The high loading of Ni–N_4/C–NH_2 (5.51 wt%) allowed for amplifying

to a gas-fed flow cell, as shown in Fig. 2d.[65] Constructed in a gas diffusion electrode, this catalyst achieved a CO partial current density (j_{CO}) of 447.6 mA cm^{-2} with almost 90% FE_{CO} at 1.0 V, where the remarkable j_{CO} in the flow cell was 7-fold that in an H-type cell, indicating the superiority of flow cell configuration.[65] Despite the exciting breakthrough in practical application, the poor long-term stability in this work caused by carbon paper used in the gas diffusion electrodes calls for the development of devices with better operation. The MEA cell designed was a good example as it realized 20 h of continuous operation on Ni-SACs at a high current density (85 mA cm^{-2}) with the FE_{CO} maintained at ~100%.

Furthermore, another insightful direction toward industrial scale-up is the type of electrolyte used in the CO_2RR system, which is of great significance, but has always been ignored. The concentration, pH and cationic species of electrolytes influence the product composition, which has been widely studied for bulk or nanostructured inexpensive metals (especially Cu).[66,67] In the very few studies that have involved SACs, an atomically dispersed Cu catalyst was shown to reduce CO_2 to ethanol with a high FE of 55% under optimized electrolyte conditions (0.1 M $CsHCO_3$). Normally, Cu-SACs rarely generate multi-carbon products such as CH_3CH_2OH or C_2H_4 due to the isolated active sites are hardly affordable for C–C coupling, which is the only route to form C_2 intermediates.[68] The appearance and then disappearance of the Cu–Cu peak in *operando* XAS analysis reveals that single metal sites are converted into Cu nanoparticles at −1.2 V and reversibly recover into SACs after electrolysis. Thus, CO_2 is catalyzed by temporarily aggregated Cu atoms and the synergistic effect boosts ethanol production. In addition, the influence of electrolyte cations has been investigated, where 0.1 M $CsHCO_3$ demonstrates the best selectivity toward ethanol and suppresses activity toward the HER (Fig. 2e) due to the formation of a large cation stabilized active Cu(I) species.[69] Overall, more efforts are needed to be put in toward this crucial research direction of cell configuration development, as well as electrolyte improvement.

2.4 Cu-based SACs

Cu-based SACs are a class of electrocatalysts that have great potential to obtain more favorable products. The unique properties of Cu for the CO_2RR have prompted researchers to conduct deeper investigations on C_2 and C_{2+} products, as valuable chemicals. In contrast, SACs with other metal centers normally generate CO or formate as products, while in several cases, highly reduced chemicals such as methanol can be produced.[70–72] A recent report demonstrated that 4.9%$_{mol}$ Cu–N_x–C SACs obtained at 800 °C favored C_2H_4 formation, while a lower concentration of Cu atoms (2.4%$_{mol}$) was inclined to form CH_4.[73] Besides the importance of the implementation of high-loading SACs being reaffirmed, the preferential products prove that the adjacent Cu active sites can work synergistically when they are close enough to one another. This enhanced result was supported by DFT calculations that showed that the porous C_2N layer supported Cu dimers exhibit excellent activity for the CO_2RR, with methane and ethylene being the main products.[74] A groundbreaking study demonstrated that Cu–pyrrolic-N_4 active sites could help to stabilize $COCOCH_3^*$ intermediates for acetone production. The proposed reaction pathway for acetone investigated *via* DFT calculations and experiments showed that the synergy between Cu and coordinated pyrrolic N led to further C–C coupling toward a C_3 species.[75] Copper doped into other metal SACs can also improve their CO_2RR selectivity. For example, by introducing Cu into Ni-SACs to form a Ni_9Cu outer layer, the adsorption energy of H* can be tuned, thus contributing toward the suppression of the HER.[76] The change in the electronic structure from the difference in the electronic density of state (DOS) was explored, as shown in Fig. 2f. The Cu addition upshifts the d-band center of Ni, which coincides well with the experimental results that Ni–Ni_9Cu exhibits a high FE_{CO} of 97%.

2.5 Metal valence

Besides its determining role in center metal selection, valence is a non-negligible factor in the electronic structure of SACs. Two valence states of Fe-SACs on carbon supports were used to explore how valence state affects the catalytic efficiency. As the valence may change during the electrocatalysis, *operando* X-ray absorption spectroscopy was used to confirm the oxidation state of the Fe ions. The results showed that Fe maintained a +3 valence during the CO_2RR, which exhibits better stability, lower onset potential, higher j_{CO}, and a higher turnover frequency (TOF) than its Fe^{2+} counterpart (Fig. 2g and h).[77] This superior ability can be attributed to the Fe^{3+} ions being stabilized *via* coupling with pyrrolic N, resulting in a $Fe^{3+/2+}$ state and a lowering of the CO_2RR potential. However, results from another study presented that Fe^+ coordinated with four pyrrolic nitrogen atoms was identified as the reactive center during the CO_2RR. The monovalent Fe species emerged when potential was applied to catalysts with a relative content of ~17.1% (−0.9 V *vs.* RHE) and disappeared after electrolysis.[78] These inconsistent results may originate from the complexity of the geometric and electronic structure of the single-Fe-atom sites, which require advanced *operando* characterization, and this will be discussed in detail in the section on spectroscopy.

3. Insights into the atomic structures of active sites

SACs can be considered as a conceptual bridge between heterogeneous and homogeneous catalysts due to their unique geometry configuration, high stability, designable active species, and the ability to clarify the structure–activity relationship at the atomic and molecular levels.[79] However, it should be noted that the catalytic sites never involve only single metal atoms. The adjacent atoms are non-trivial in that they can influence the CO_2RR performance, as the doping elements can tune the coordination environment and the carbon-based framework supports the basic conductive function. Until now, carbon-based non-noble metal-based SACs have been extensively reported and have provided an opportunity to clarify the mechanism of inter-atomic interactions. Insights gained from

these studies are based on simplified molecular models. In this section, the regulation of coordination structures, including coordination numbers, heteroatom types and vacancy/edge defected designs, will be discussed. Moreover, we will focus on the recent progress on diatomic models toward C_2 products in the fourth section.

3.1 M–N–C structure

Fig. 3 illustrates all the possible M–N–C structures with different coordination numbers and configurations of N atoms. Nitrogen is a low-cost, earth-abundant element, which creates an electron-rich environment to anchor metal atoms. Different coordination environments regulate the electronic properties of single metal atoms. A series of carbon-based SACs with coordination structures of isolated M–N–C as typical catalytically active sites have been widely studied. Plenty of studies have explored how the different coordination numbers on graphene supports affect the CO_2RR performance. Representative models of the active sites are shown in Fig. 3. In general, the coordination number can be regulated by the pyrosis temperature but it is uncontrollable to obtain the same active motifs.[25,32,80,81] On the other hand, molecules like porphyrin (TPP)[82] or phthalocyanine (Pc)[83] as well as periodic N-containing substrates like graphitic carbon nitride (g-C_3N_4)[84] or holey nitrogen-doped graphene (C_2N)[85] are usually used to help develop SACs with uniformity.

Despite a diversity of synthesis strategies, controversies about the most active M–N–C site still exist. DFT calculation results have predicted that a single Ni metal atom anchored with three carbon and one nitrogen (Fig. 3a) exhibits the best catalytic activity and selectivity toward the CO_2RR.[86] The computational results demonstrate that the introduction of one nitrogen (1N) decreases the CO* desorption barrier and yields better CO productivity on a Ni–C_3N_1 site than a Ni–C_4 site. Meanwhile, the high charge capacity of the 1N site allows for the carrying of more charge to facilitate the reduction process. In comparison, a lower work function at the charge-neutral state restricts the charge capacity of 4N counterparts when they are charged to the same final Fermi level. Nonetheless, other studies from an experimental perspective reached different conclusions. SACs with different coordination numbers (M–N_2, M–N_3, M–N_4, M–N_5) on carbon-based supports have been evaluated according to several aspects. Frequently mentioned is coordination unsaturated M–N_x, which is more reactive than M–N_4 motifs during the CO_2RR due to the suppressed HER activity and lower free energy of the formation of the *COOH intermediate.[87] For example, a graphene-supported Cu–N_2 site (Fig. 3b) has shown superior activity than Cu–N_4 sites, reaching a high FE_{CO} of 81% at −0.5 V *vs.* RHE.[88] This result can be rationalized by geometry structure differences, in that the bond lengths of Cu–N_2 sites are shorter than those of Cu–N_4, which is beneficial toward promoting electron transfer from the central metal to the activated *CO_2. Another example compared the activity of Co–N_x–C (x = 2, 3, 4) SACs pyrolyzed at different temperatures and Co–N_2–C was found to exhibit the best CO_2RR performance, with a record TOF value of 18 200 h^{-1}.[80] The characterization of three samples with different coordination numbers was presented in detail and the N_2 coordination state was reconfirmed upon NH_3 treatment. The M–N_3–C sites (Fig. 3c) also show advantages for improved CO_2RR

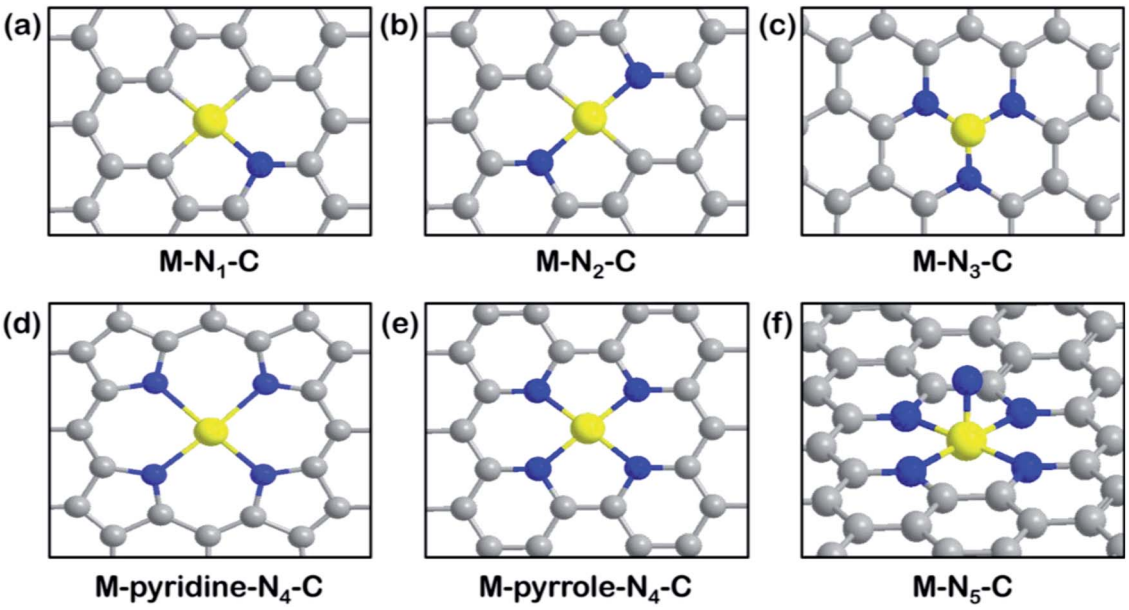

Fig. 3 Overview of M–N–C structures. Schematic illustration of (a) M–N_1–C. Reproduced with permission from ref. 86, copyright 2020, American Chemical Society. (b) M–N_2–C. Reproduced with permission from ref. 88, copyright 2019, Wiley-VCH. (c) M–N_3–C. Reproduced with permission from ref. 81, copyright 2018, Wiley-VCH. (d) M–pyridine-N_4–C. Reproduced with permission from ref. 91, copyright 2020, Springer Nature Publication. (e) M–pyrrole-N_4–C. Reproduced with permission from ref. 77, copyright 2019, Science. (f) M–N_5–C molecular models. Reproduced with permission from ref. 93, copyright 2019, Wiley-VCH. (M: yellow; C: grey; N: blue).

performance. Ni–N_3–C exhibits much lower free energy for the first electronic step (activation of CO_2 to *COOH) than Ni–N_4–C, from computational investigations, making it optimal to serve as the active sites.[81] In recent work, Mn–N_3–C_3N_4 on carbon nanotubes (CNTs) was exploited for the CO_2RR and was found to exhibit better performance (FE_{CO} of 98.8% and j_{CO} of 14 mA cm^{-2} at an overpotential of 0.44 V) than previously reported graphene-supported Mn–N_4 SACs.[89] *In situ* XAS results indicated that the electron redistribution of the Mn active site after CO_2 adsorption increased the Mn oxidation state, which then returned to its original state after one CO_2 reduction cycle, indicating that the CO_2RR takes place at the Mn–N_3 sites. The calculated local density of states on Mn–N_3–C_3N_4 exhibit a closer distance between the d-band center and the Fermi level than Mn–N_4–C models, which is favorable toward CO_2 binding and activation.

However, based on different calculation models and imposed forces, along with different rate-determining steps, the most reactive sites have been identified as M–N_4 or M–N_5 in some published studies.[90] For instance, we reported that Ni–N_4 exhibits the best catalytic activity for the CO_2RR using grand canonical potential kinetics (GCP-K) calculation methodology, which was found to be in good agreement with experimental results showing that FE_{CO} reached ~100% and j_{CO} was 40 mA cm^{-2} at −1.05 V *vs.* RHE.[91] The HER performance was shown to be correlated to coordinated C numbers from three aspects (FE_{CO}, TOF, and Tafel slope) and we found that the Ni–N_4 sites are superior to Ni–N_2 and Ni–N_3. A similar conclusion has been drawn by other research teams, in that Co–N_4 SACs exhibit higher FE_{CO} and j_{CO} values than coordination unsaturated Co–N_{4-x} over a full range of applied potential from −0.5 to −1.0 V *vs.* RHE.[92] On the other hand, it is critical to distinguish between M–N_4 motifs constructed using different N-containing ligands (Fig. 3d and e), as pyrrolic N ligands might stabilize Fe^{3+} for faster CO_2 adsorption, whereas pyridinic N ligands exhibit the opposite effect in that Fe^{3+} ions are reduced to Fe^{2+} ions at −0.1 to −0.2 V *vs.* RHE.[77]

Axial coordination of addition N to the M–N_4 plane to form M–N_5 sites has been demonstrated to be an effective way to promote the CO_2RR. As shown in Fig. 3f, the axial ligand tunes the electronic properties of the central metal, especially the valence state. Fe–N_5 SACs have been prepared by dispersing Fe–N_5 on N-doped graphene and XAS tests were used to identify that the Fe–N_5 sites exhibit higher oxidation states than typical Fe–N_4 sites.[93] A subsequent computational investigation determined that boosting d electron transfer from Fe to the additional N led to a weaker binding strength of *CO, thus facilitating the final CO production. Another related study reported that the valence of central Co in a five coordinated N species was higher than that of a Co–N_4 analog.[94] The coordination affinity is beneficial to the rapid formation of *COOH as well as CO desorption. All these studies emphasize the influence of different coordination numbers on the catalytic performance of M–N–C toward the CO_2RR.

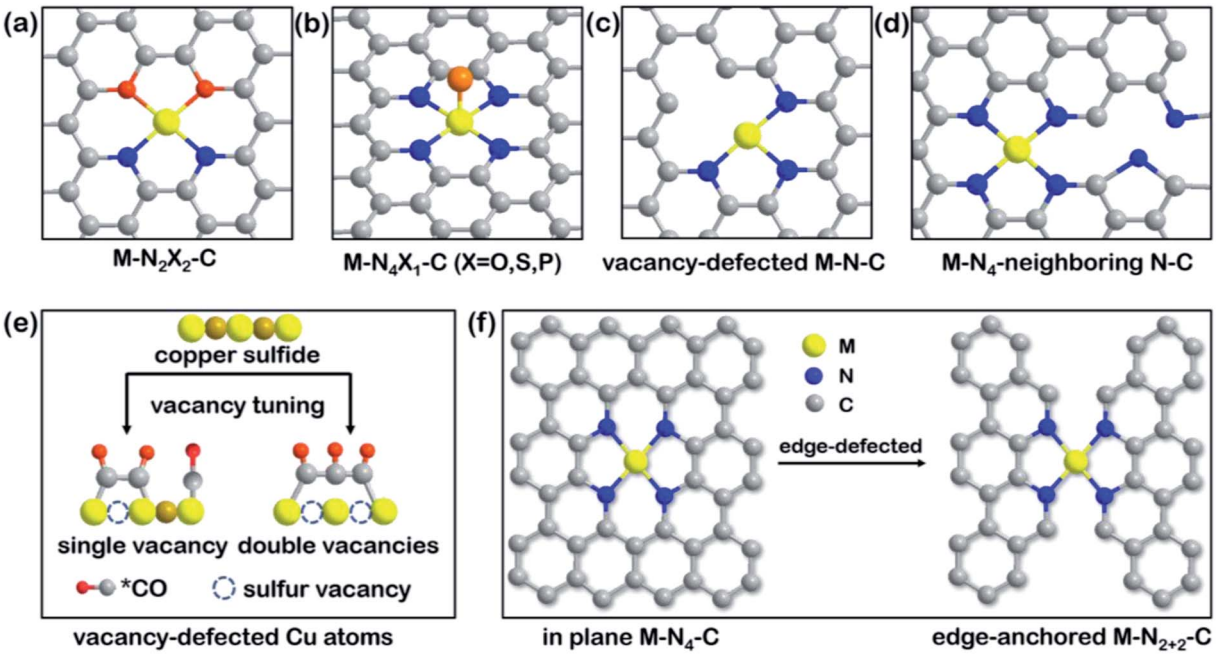

Fig. 4 Overview of model engineering of SACs. Schematic illustration of (a) N-heteroatom co-doped M–N_2X_2–C. Reproduced with permission from ref. 96, copyright 2021, Springer Nature Publication. (b) Axial-coordinated M–N_4X_1–C. Reproduced with permission from ref. 100, copyright 2021, Wiley-VCH. (c) Vacancy-defected M–N–C. Reproduced with permission from ref. 104, copyright 2020, Wiley-VCH. (d) Non-coordinated M–N_4-neighboring N–C models. Reproduced with permission from ref. 105, Copyright 2021, Elsevier. (e) Mechanism of C_3 product formation by tuning from a single sulfur vacancy to double vacancies in copper sulfide. Reproduced with permission from ref. 106, copyright 2021, Springer Nature Publication. (f) Edge-defected design of in-plane M–N_4–C and edge-anchored M–N_{2+2}–C. Reproduced with permission from ref. 107, copyright 2019, Royal Society of Chemistry. Model engineering such as heteroatom co-doping or creating vacancies/edges introduces diverse electronic states for SACs.

3.2 Heteroatom co-doping

Fig. 4 illustrates an overview of representative engineering models, such as heteroatom co-doping and vacancy or edge defects. Due to the difference in electronegativity of common non-metals (like N, O, P, S), it is feasible to break the symmetry of electronic distribution by modulating the types of coordination atoms among catalytic centers.[95] Atomic-level tuning is sensible for SACs as electronic redistribution is effective, while precise regulation is quite challenging. In recent work, Cu–N_2O_2 (Fig. 4a) SACs were prepared with the help of copper disodium EDTA on carbon dots and the resulting catalysts exhibited extraordinary selectivity toward CH_4.[96] The central metal experienced an oxidation state change from Cu^{2+} to Cu^{+}/Cu^{0} due to the strong covalent interactions between Cu^{2+} ions and the O-containing ligand, which decreased the Cu 2p binding energy. The less positive charge density of the Cu atoms in Cu–N_2O_2 sites rationalized the lower energy barriers of all of the CO_2RR intermediates and the higher adsorption energy for *H than typical Cu–N_4 sites. Apart from the chelate-assisted method, well-defined heteroatom co-doping can also be achieved by modifying the molecular structure directly. By breaking the perfect D_{4h} symmetry of tetraphenylporphyrin (N_4-TPP) to obtain 21-oxatetraphenylporphyrin (N_3O-TPP), the structural uniformity of N_3O has been shown to became an ideal framework for the anchoring of single Ni atoms.[97] DFT calculations revealed that the polarization of O-doping lowered the valency of the Ni center and led to a stronger Ni–C bond to stabilize *COOH intermediates. S substitution in the porphyrinic framework produced a similar effect, reported in another theoretical study.[98] By replacing two opposable pyrrole N atoms with S atoms, the electronic optimization of the Fe center showed better intramolecular electron transfer ability than Fe–N_4. Moreover, N, S co-coordination resulted in a weaker CO binding energy for efficient CO production and a decreased limiting potential that surpasses those of most reported SACs. Other co-doping elements, such as P, S in Co–N_3, for electronic density modulation of Co-SACs has also proven the importance of heteroatoms.[99]

The axial coordination of heteroatoms results in a similar atomic structure to M–N_5, as depicted in Fig. 4b, but leads to different CO_2RR performance. A rarely reported metal, Cd, was used to prepare Cd–N_4S_1 SACs for the CO_2RR, the catalytic activities of which were compared with that of Cd–N_5.[100] The straightforward comparison of axial atoms showed that even though both active sites effectively boost CO_2RR, the high spin density and charge delocalization of S remarkably decrease the highest free energy barrier on Cd–N_4S_1 compared with that on Cd–N_5. Despite the Cd atom preferring to form five coordination structures due to its large atomic radius, the enhancement of the added axial heteroatom has also worked in other systems. For example, diphenyl sulfide was used as an axial ligand to promote interfacial electron communication, resulting in a 1.5 times increase in the TOF (2.4 s^{-1}) of Co–N_4S_1 at −0.87 V compared with that of pristine Co–N_4.[101] In another study, O coordinated with Fe–N_4 from an out-of-plane position and was shown to maintain excellent stability at low overpotentials. DFT calculations showed that *CO could be desorbed from the Fe–N_4O motifs easier than from Fe–N_4 and Fe–N_5 sites.[102] Accordingly, regulated coordination models based on other elements are conducive to the CO_2RR and should be considered for improving electrocatalysts.

3.3 Vacancy/edge defects

As is known, defect structures are appropriate anchoring sites for single metal atoms.[41,103] Strategies to create and control vacancy or edge defects around metal centers has attracted increasing attention. Pyrolysis, as the most used method to prepare SACs, can also be applied to create controllable vacancies in carbon substrates. For instance, vacancy-defected Ni–N_3–V SACs (Fig. 4c) could be obtained by taking advantage of the easy evaporation of coordinated oxygen at high temperatures.[104] Vacancy defects provide moderate free energies for CO_2 activation and CO desorption in comparison to defect-free Ni–N_3, as shown in Fig. 3c. Thus, the manageable structure of Ni–N_3–V exhibits the best catalytic performance, with a high j_{CO} (65 mA cm^{-2}) value at −0.9 V *vs.* RHE. The vacancy beyond the adjacent atoms also modulates the catalytic activity, so that the non-coordinated N in vacant carbon support can tune the electronic properties of the M–N_4 motif, as illustrated in Fig. 4d.[105] The authors of the study demonstrated a surprising discovery that the Ni atom in the Ni–N_4 species was no longer the active site, with the four adjacent N atoms being responsible for catalyzing the CO_2RR. Due to the pyrrolic-N in the neighboring Ni–N_4 site inducing electron transfer from Ni 4s orbitals to adjacent N 2s orbitals, the electron-rich N facilitated the *COOH formation and then boosted the CO_2RR performance. This latest study presents the impact that vacancy adjustment has on preferred electrocatalytic products by tuning the sulfur vacancies of copper sulfide (Fig. 4e).[106] It was found that the single vacancy could not support CO–OCCO coupling due to the strong electrostatic repulsion of three *CO intermediates. In contrast, the double adjacent coplanar vacancies enabled the formation of a polyline OC–COCO trimer with a decreased adsorption energy of −0.23 eV. The advantages like the reduced steric hindrance and enriched negative charge density of double vacancies promote CO_2-to-C_3H_7OH conversion. Although this example is not about SACs, the significance of vacancies should be understood and more SACs models with multiple controllable vacancies are encouraged to be developed in the future.

Edge defect engineering regulates the electronic structure of the active sites indirectly. Two different structural models, in-plane Ni–N_4–C_{10} and edge-anchored Ni–N_{2+2}–C_8, were explored and their CO_2RR performance compared (Fig. 4f). Although their coordination numbers of N were the same, the Ni–N_{2+2}–C_8 motif with edge defects contained a dangling bond for faster dissociation of the C–O bond in *COOH while Ni–N_4–C_{10} did not, according to DFT calculations.[107] However, the difference between these two structures was not well revealed in the experiments. In another study, edge-located unsaturated N was shown to play a role in anchoring single Ni atoms and increasing electron density, resulting in an excellent TOF, comparable to those of noble metal-based catalysts, such as

those containing Ag.[108] Aberration-corrected scanning TEM confirmed that Ni single atoms were primarily anchored on the edge of defective graphene. Moreover, DFT demonstrated that the in-plane Ni–N_3 site was unfavorable for CO desorption, while the edge-anchored analog with intermediate adsorption strength exhibited the optimal catalytic activity based on the Sabatier principle.

3.4 Bimetallic SACs

Although traditional SACs have been shown to exhibit great performance in the electrochemical CO_2RR, the isolated metal atoms work independently with each other. However, the electronic nature of each non-noble metal limits further improvement in terms of higher efficiency and deep reduction products. For instance, Fe-SACs exhibit superior onset potential for CO_2-to-CO reduction but are burdened by the strong binding energy of CO, while Ni-SACs show high current density but suffer from the sluggish kinetics of the first PCET process.[109,110] Researchers have further discovered that neighboring single atoms could affect CO_2RR performance when they are close enough, as they optimize the adsorption energy of intermediates or even lead to the formation of a C_2 product.[73] Accordingly, bimetallic SACs with tunable collocation and molecular models have emerged as a new frontier in electrocatalysis.

Fig. 5 illustrates two dual-atom catalyst models and the latest work on bimetallic SACs for the CO_2RR. The proposed structures of bimetallic SACs in recent work, M_1M_2–N_8–C and M_1M_2–N_6–C, are shown in Fig. 5a and b. M_1M_2–N_8–C is composed of two adjacent but separate M–N_4-type SACs with two different metal centers. Recently, NiSn atomic pair catalysts supported on N-doped carbon nanosheets with an M_1M_2–N_8–C structure

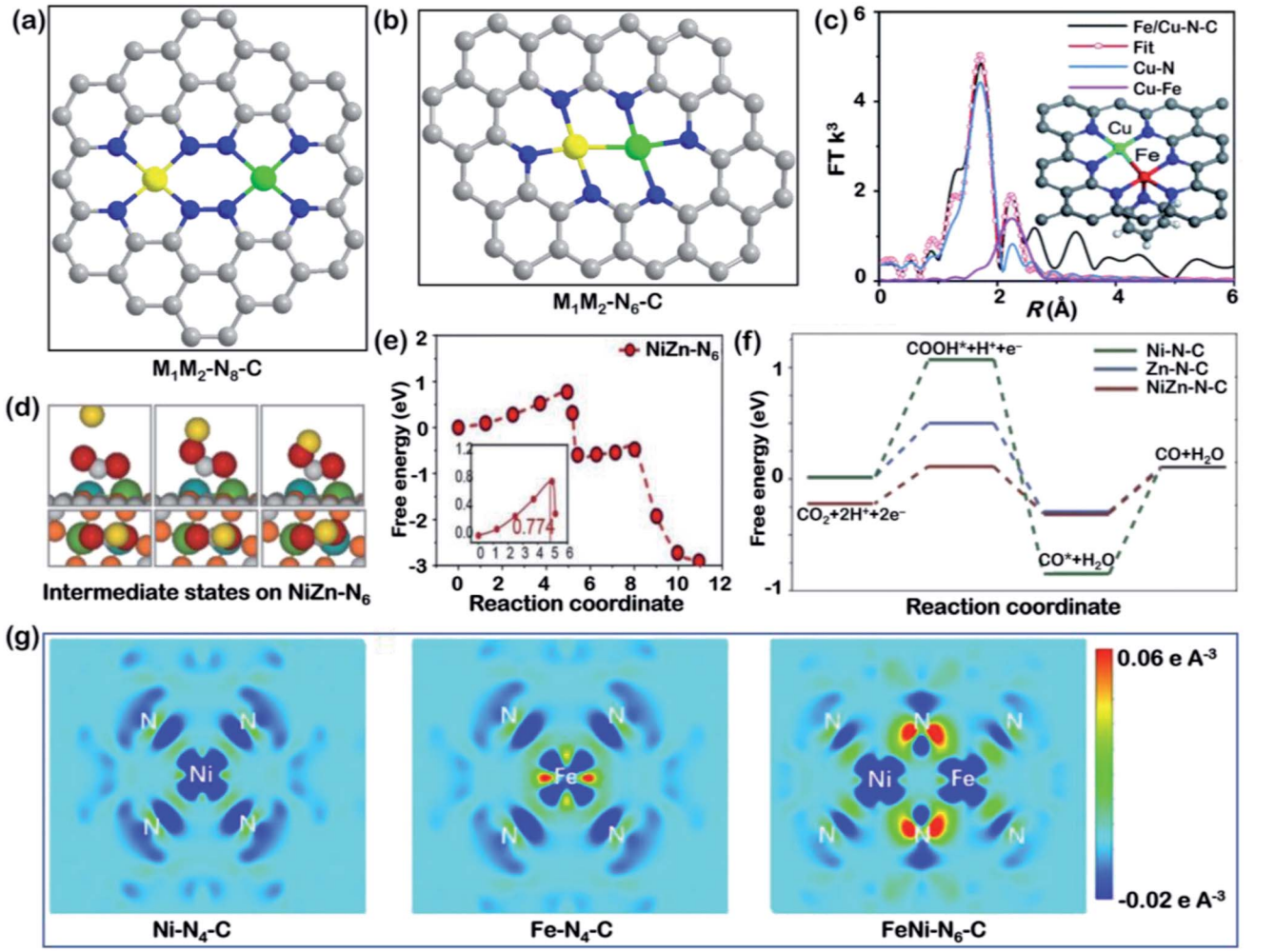

Fig. 5 Bimetallic SACs. Schematic illustration of (a) M_1M_2–N_8–C and (b) M_1M_2–N_6–C models (M_1: yellow; M_2: green; C: grey; N: blue). (c) EXAFS fitting for FeCu–N_6–C in R space; inset: a proposed model for FeCu–N_6–C, where black, blue, red, and indigo represent C, N, Fe, and Cu atoms, respectively. Reproduced with permission from ref. 115, copyright 2021, Royal Society of Chemistry. (d) Diagrams of the atomic structure and energy changes of the starting, intermediate, and final states of the CO_2RR, and (e) CI–NEB-calculated *COOH on NiZn–N_6–C reaction kinetics, and (f) the free energy of each intermediate state on the metal atom sites in Zn–N–C, Ni–N–C, and ZnNi–N–C. Reproduced with permission from ref. 117, copyright 2021, Wiley-VCH. (g) The differential charge density maps of Ni–N_4–C, Fe–N_4–C, and NiFe–N_6–C. From aquamarine to orange indicates the transition from electron depletion to accumulation. Reproduced with permission from ref. 118, copyright 2021, Springer Nature Publication.

were utilized for the CO_2RR.[111] The separate configurations of Ni–N_4 and Sn–N_4 were proven by XPS and XAFS analysis, as no Ni–Sn bond was observed. The excellent overall FE and TOF for CO_2-to-formate transition could be attributed to the cooperation of dual metal centers, in which Ni–N_4 favors CO_2 adsorption and Sn sites boost *OCHO intermediate formation. The detached bimetallic SACs provide a promising method to realize syngas production with a controllable CO/H_2 ratio for typical downstream thermochemical reactions. In another study, CoNi–N_8–C dual-atom SACs for syngas evolution were demonstrated to exhibit a high total current (>74 mA cm^{-2}) with a tunable CO/H_2 ratio of 0.23–2.26 by controlling the ratio between Co and Ni.[112] DFT revealed that Co–N_4 and Ni–N_4 sites selectively promoted the HER and CO_2RR, respectively, and the reaction pathways on coexisting CoNi dual atoms were similar to those of single metal sites. Thus, the regulation of product composition was able to be achieved by tuning the Co/Ni ratio. Similarly, a synergistic effect was observed on Ni paired with Fe in an M_1M_2–N_8–C model.[113] The introduction of Ni changed the energy barrier for the CO_2RR reaction and increased the stability of Fe-SACs due to strong CO* adsorption. Moreover, differing the configuration of bimetallic centers changes the rate-determining step, as evidenced by the calculated DOS after COOH* and CO* adsorption.

On the other hand, the M_1M_2–N_6–C structure contains direct metal–metal coupling within the diatomic molecular model (Fig. 5b). A series of DFT simulations were conducted for this dual atom structure supported on graphene.[114] Based on multiple combinations of transition metals with different electronegativity, Cu/Mn, Ni/Mn and Ni/Fe were presented that showed superior activity for the CO_2RR compared with Au (211). These three diatomic catalysts break the scaling relationship between COOH* and CO* adsorption strength and serve as a guide to design optimal bimetallic SACs. In particular, a unique seven coordinated structure, N_4Fe–CuN_3, was reported by He and coworkers very recently, as illustrated in the inset model in Fig. 5c.[115] The fitting results of EXAFS spectra (Fig. 5c) suggested the existence of Cu–Fe coordination. The diatomic catalyst exhibited a synergistic effect and showed a much higher TOF than Fe–N_4 and Cu–N_4 over a wide potential range of −0.4 to −1.1 V *vs.* RHE. Its enhanced catalytic activity arose from the closer distance between the d-band center of N_4Fe–CuN_3 to the Fermi level than those of Cu- and Fe-SACs. Except for this example, most heteronuclear systems leads to bimetallic SACs with six coordinated nitrogen atoms.[116] The latest reported work involved the study of atomically dispersed Ni–Zn catalysts with an M_1M_2–N_6–C structure from both kinetical and thermodynamic perspectives.[117] In terms of kinetics, the authors utilized the climbing image nudged elastic band (CI-NEB) calculation to study the reaction process, with the starting, intermediate, and final states, as depicted in Fig. 5d.[117] The calculated free energy of *COOH revealed a reduced barrier on the Ni–Zn bimetallic SACs (Fig. 5e). In terms of thermodynamics, ZnNi–N–C was shown to be more selective toward the CO_2RR than Zn–N–C and Ni–N–C due to its lower free energy for COOH* formation (Fig. 5f). A decreased gap between the d-band center of the Ni 3d orbitals and the Fermi level was also observed in this work. The activation energy of CO_2 hydrogenation on bimetallic sites was significantly lower than on the other two single-atom configurations, explaining the efficient CO_2RR pathway on ZnNi–N_6–C sites. For another NiFe–N_6–C catalyst, the electronic structures of single-atom and diatom catalysts were visually expressed using differential charge density maps (Fig. 5g).[118] These maps indicate that, in a bimetallic catalyst, more electrons are delocalized around the coordinating N between Ni and Fe with electrons partially transferred from an Fe atom. The electron redistribution leads to a higher oxidation state of Fe and therefore enhances CO_2 activation and CO desorption.

Besides the dual-atom sites built in a relatively fixed atomic structure of active sites, several bimetallic SACs comprise two types of SACs. Isolated Zn and Co atoms coordinated on N-doped carbon black were prepared *via* pyrolysis and achieved a FE_{CO} of 93.2% and j_{CO} of 26 mA cm^{-2} at −0.5 V *vs.* RHE.[119] The electronic interaction between neighboring Zn/Co active sites was demonstrated by XANES spectra analysis, but the complex and uncertain diatomic structure may lead to less persuasive simulation results. Another Zn/Co tandem catalyst demonstrated good CO_2RR performance beyond two-electron transfer.[120] Experiments and calculation results revealed a two-step mechanism in which CO_2-to-CO transfer preferentially takes place on the Co atom first and then CO diffuses to a Zn site and is further reduced to CH_4. The high FE toward CH_4 (15%) can be attributed to the Co site enhancing the adsorbed *H over the coordinated N of Zn–N_4.

Despite the various molecular models based on single atoms or dual atoms that have been investigated, factors beyond the metal-containing active sites can also determine the reaction pathways. For example, the immobilization of Co phthalocyanine (CoPc) onto a conductive CNT led to a six-electron transfer process from CO_2 to methanol in comparison to a two-electron reduction to CO for homogeneous CoPc.[71] It was observed that the close contact of molecular CoPc with the conductive CNT/electrode partially contributed to the high FE toward methanol due to the high degree of electronic communication. The electrocatalytic nanocarbon thus plays a significant role that should not be ignored.[121] Furthermore, SACs derived from MOFs or COFs can adsorb CO_2 gas due to their porous nature, which affects the reaction results.[58] To sum up, research on active molecular models is very important, but this should not be the sole point by which to evaluate a catalytic system. Standards and protocols for experimental and theoretical data acquisition are highly recommended to identify the intrinsic mechanism of SACs toward the CO_2RR.

4. Insights from spectroscopy

The atom-level identification of SAC structures is difficult but essential for further mechanism investigation. Widely used microscopies such as scanning transmission electron microscopy (STEM) can be used to visually determine surface morphology, but they cannot provide detail on the explicit structural and electronic properties of SACs.[23] The molecular models and proposed reaction pathways based on theoretical calculations require experimental evidence for confirmation.

The urgent demand for advanced spectroscopic characterization has brought about breakthroughs in the field of the CO_2RR.

4.1 XAS

X-ray absorption spectroscopy (XAS), including X-ray absorption near-edge structure (XANES) and extended X-ray absorption fine structure (EXAFS), is a remarkably useful technique in characterizing SACs. An XANES spectrum can be used to determine the chemical valence state and electronic configuration of the target element, while pre-edge features can offer information such as bond angles.[122,123] EXAFS can be used to probe the local structure and give us valuable spatial insight into the geometric structure and coordination environment.[122] Specifically, fitting the results from Fourier-transform EXAFS (FT-EXAFS) can help to infer the interatomic distances between the absorber and scattering atoms and coordination numbers.[121,122] Fig. 6a shows the different valence states of two Cu–N–C catalysts prepared at different pyrolysis temperatures and a comparison of their Cu K-edge XANES spectra with reference samples.[73] It can be seen that the main peak of the Cu-SACs shift toward the middle energy region between the Cu_2O and CuO references, indicating that the Cu atoms are in higher oxidation states of Cu(I) or Cu(II). The atomic structure investigated by FT-EXAFS confirmed the presence of Cu–N bonds and the existence of Cu–Cu bonds in the annealed samples, suggesting that the Cu atoms are isolated and coordinated to N atoms (Fig. 6b). Li and coworkers explored antimony (Sb) single atoms dispersed on N-doped carbon for the CO_2RR, which can efficiently produce formate as a product. N K-edge soft XAS measurements were used to identify the electronic structure of the N and C species surrounding the Sb atoms, revealing the existence of pyridinic N, pyrrolic N and graphitic N.[124,125] The ultra-high sensitivity of XAS makes it a useful tool with which to figure out the electronic state of target metal atoms and ligand species.

Wavelet-transform (WT)-EXAFS can be used to discriminate the diverse back-scatterers in the overlapped signals and allow us to interpret EXAFS spectra visually.[126] As shown in Fig. 6c, the WT-EXAFS images of NiSn diatomic catalysts and Sn-SACs exhibit a similar maximum intensity at 6 $Å^{-1}$, which can be assigned to Sn–N contributions.[111] The maximum intensity of Sn–Sn located at 8.6 $Å^{-1}$, as displayed for the Sn foil, suggests that Sn in both the NiSn catalyst and Sn-SACs exist in the form of being independently dispersed. In another study, a similar method was used to recognize the Cu single-atom dispersity of Cu–N–C by comparing the highest WT positions of CuPc and Cu foil.[127]

The active centers under electrolysis are not always the same structure as what is detected by *ex situ* spectroscopies, as the isolated sites may go through geometric or electronic evolution. The identification of real active sites under working conditions has encouraged researchers to focus on *in situ* and *operando* techniques. The abovementioned example by Fontecave and colleagues reported that the Cu–N_4 sites were reconstructed into small Cu nanoparticles to enhance CO_2RR toward deeply reduced products.[69] This geometric change was monitored by *operando* XAS and explained why their Cu-SACs could produce chemicals beyond CO. *In situ* XANES spectra can also help researchers to explore the evolution of different Cu oxidated species during the CO_2RR. As shown in Fig. 6d, the appearance of Cu(I) and Cu(0) peaks under increased reduction potentials indicates that Cu changes oxidation state during working status while in open-circuit voltage (OCV), where Cu(II) was the dominant spectral feature.[128] This transition was found to be reversible upon switching the potential back to 0.64 V, and the XANES spectrum was almost back to that of the OCV state. Combined *in situ* XAS and electrochemical results give us valuable insight to link the CO_2RR performance to realistic catalytic sites.

4.2 Optical spectroscopies

In situ attenuated total reflection-infrared (ATR-IR) spectroscopy was introduced to characterize the reaction intermediates, and the latest work used this technique to monitor *COOH adsorbed on active sites *via* the vibration of C═O stretching (Fig. 6e).[53] The increasing peak intensity at 1400 cm^{-1} achieved a maximum at −0.97 V, indicating that *COOH formation could be regarded as RDS for the CO_2RR on fluorine-doped Ni-SACs. *Operando* Raman spectroscopy has also been used to detect the oxidation states of active moieties during the CO_2RR process. Actually, the aqueous electrolyte in the CO_2RR system is more suitable for *operando* Raman spectroscopy rather than *operando* IR spectroscopy due to the low scattering of water in Raman spectra.[129] By utilizing *operando* Raman spectroscopy, Liu and coworkers found that the vibration peak of Ni–N (at ~244 cm^{-1}) shifted to a lower wavenumber when the applied cathodic potential was above 0.57 V, implying a weaker interaction between the Ni atom and coordinated N atoms.[130] This redshift could be attributed to the *in situ*-formed Ni^+ from Ni^{2+} reduction *via* the addition of an electron to a Ni 3d orbital. The monovalent Ni unraveled by *operando* Raman spectroscopy provided experimental proof for the proposed reaction mechanisms of the CO_2RR.

4.3 Mössbauer spectroscopy

Mössbauer spectroscopy is a precise technology that is used to probe the elemental spin, oxidation states and geometric symmetry of Mössbauer isotopes such as ^{57}Fe, ^{119}Sn, *etc.*[129] In the field of SACs for the CO_2RR, Mössbauer measurements have been extensively used to identify Fe species with different coordination and electronic structures. For instance, in the work done by Li and coworkers, the doublets (D1 and D2) fitted in the Mössbauer spectra are in accordance with Fe–N_x moieties wherein the metal center is in low-spin (LS) and intermedium-spin (MS) states, respectively.[123] Fontecave and colleagues exploited a series of Fe–N–C catalysts for the CO_2RR and utilized ^{57}Fe Mössbauer spectroscopy to distinguish its components, such as α-Fe and iron carbide.[131] In composition analysis by Mössbauer spectroscopy, the isolated Fe–N_4 was proven to be the active site for CO_2-to-CO conversion. *Operando* Mössbauer spectroscopy characterization can therefore provide quantitative information on the geometric structure and electronic environment of real active sites under reaction conditions. The development of *operando* Mössbauer spectroscopy on the

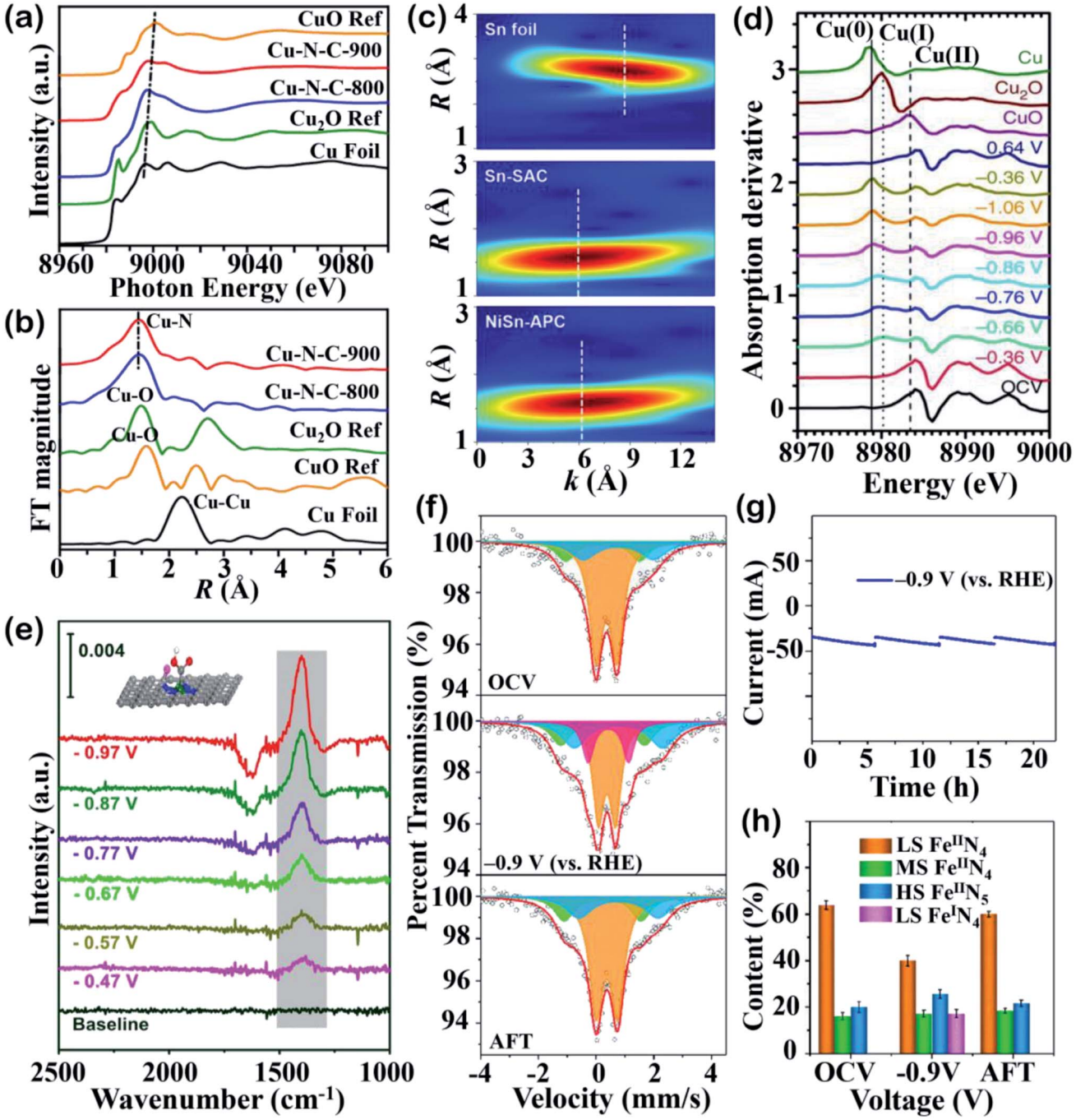

Fig. 6 Spectroscopic studies. (a) XANES spectra and (b) FT-EXAFS spectra. Reproduced with permission from ref. 73, copyright 2020, American Chemical Society. (c) EXAFS wavelet-transform (WT) images of Sn foil, Sn-SAC and NiSn-APC. Reproduced with permission from ref. 111, copyright 2021, Wiley-VCH. (d) First-order derivatives of the Cu K-edge *in situ* XANES spectra for Cu(II) phthalocyanine under electrocatalytic reaction conditions. Reproduced with permission from ref. 128, copyright 2018, Springer Nature Publication. (e) *In situ* ATR-IR spectra of Ni–N_4 SACs under increasing applied potentials in 0.5 M $KHCO_3$. Reproduced with permission from ref. 53, copyright 2021, Elsevier. (f) *Operando* ^{57}Fe Mössbauer spectra of ^{57}Fe-enriched Fe–NC–S collected under OCV, −0.9 V (*vs.* RHE), and after reaction. The orange, green, blue, and purple doublets could be assigned to LS Fe^{2+} in $Fe^{II}N_4$, MS Fe^{2+} in $Fe^{II}N_4$, HS Fe^{2+} in N–$Fe^{II}N_4$, and LS Fe^{2+} in $Fe^{I}N_4$, respectively. (g) Current–time response and (h) contents of different Fe moieties derived from Fig. 5f. Reproduced with permission from ref. 78, copyright 2021, American Chemical Society. Advanced spectroscopic techniques help to probe the atomic structure under *ex situ*/*in situ* conditions and provide experimental proof.

laboratory scale was recently achieved using a specially designed H-cell to prevent spectral interference. Steady current–time responses during *operando* Mössbauer spectroscopy measurements were obtained and the spectra were fitted with multiple doublets, as shown in Fig. 6f and g.[78] The three doublets in orange, green, and blue represent LS Fe^{2+} in $Fe^{II}N_4$,

MS Fe^{2+} in $Fe^{II}N_4$, and high-spin (HS) Fe^{2+} in N–$Fe^{II}N_4$, respectively. When applying a voltage of −0.9 V *vs.* RHE., the appearance of a new purple doublet could be assigned to LS Fe^{2+} in $Fe^{I}N_4$, which arose due to the decreased LS content, suggesting that LS Fe^{2+} in $Fe^{II}N_4$ sites experiences dynamic evolution during the electrolysis. The relative content of the four Fe species in Fig. 6h implies the *in situ* generation of LS $Fe^{I}N_4$ as a highly active site for the electrochemical CO_2RR.

5. Insights from computational studies

5.1 DFT studies on the CO_2RR

The electrochemical performance of SACs for the CO_2RR has been determined experimentally, but it remains challenging to analyze the features that determine the catalytic activity. In this regard, theoretical studies could give more insights into the reaction mechanism. Specifically, using DFT, the reaction cycle and energy barriers for each elementary step can be estimated accurately (Scheme 1). Furthermore, theoretical calculations can help to reveal the electronic structure of the active sites to determine structure–performance relationships.

Uniformly-dispersed transition metal-based SACs provide a perfect platform for acquiring a clear theoretical comprehension of the CO_2RR process. For example, the CO_2RR process by DFT calculation was investigated using a series of transition-metal based SACs, M/SV–graphene and M/DV–graphene.[132] By comparing the free energies of the first protonation step with that of the *H adsorption process, most of the SACs exhibited preferential selectivity for the CO_2RR over the competitive HER. The results indicate that the efficiency and selectivity for the CO_2RR products can be correlated to the valence electrons, where the reduction ability decreases with decreased energy at the d-level. As re-summarized in Fig. 7a, CH_4 is preferentially produced by Fe/SV and Co/SV, while the main product for Ni/DV, Cu/DV, and noble-metal (such as Pt and Pd) based catalysts is CH_3OH.[132] A similar result on the correlation between efficiency and selectivity for the CO_2RR according to the elemental properties of metals as a function of their group number has also been reported in another study.[133]

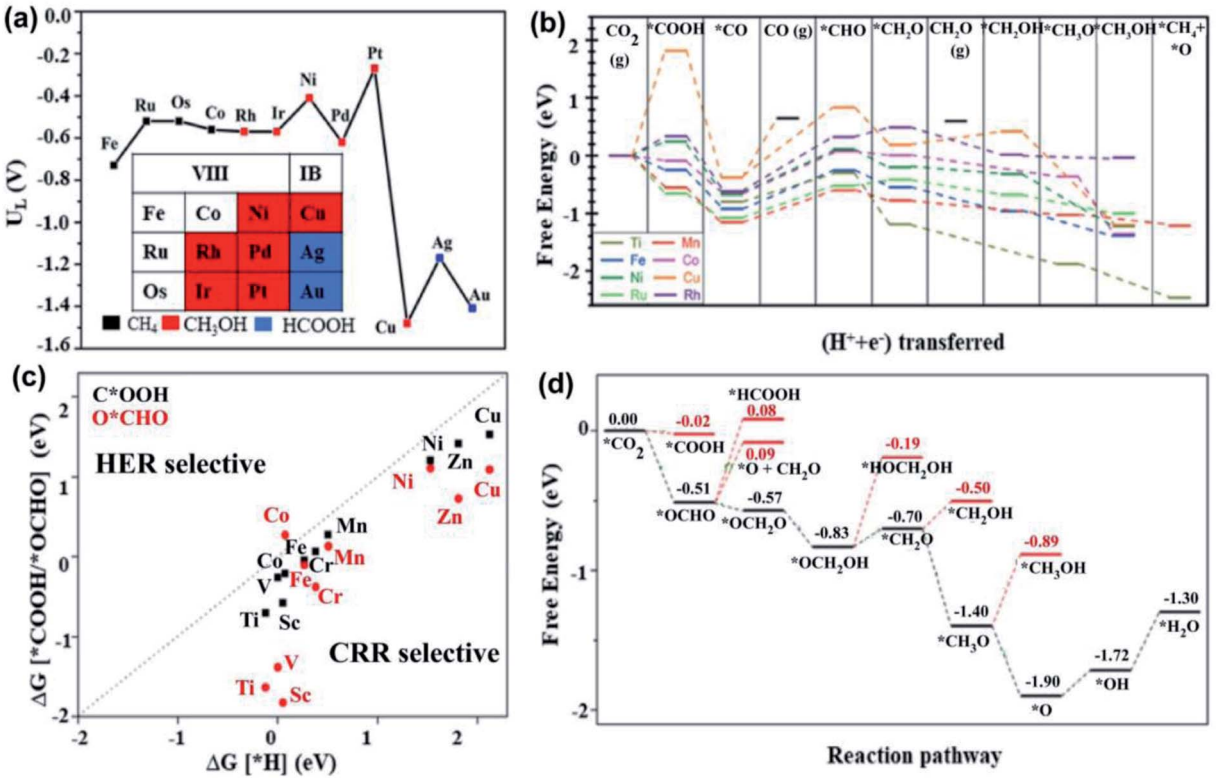

Fig. 7 DFT analyses. (a) Limiting potentials and product selectivity of the CO_2RR on various TM-based SACs anchored on graphene. The results indicate that a Ru SAC has a minimum limiting potential of −0.52 V for CH_4 production, while Pt is more prominent for the CH_3OH synthesis, and Ag, and Au preferentially produce formic acid. Reproduced with permission from ref. 133, copyright 2017, Royal Society of Chemistry. (b) Free energy profile for CO_2RR to various products on various TM@C_2N active sites. CH_4 is only produced by Ti and Mn-based SACs. Reproduced with permission from ref. 138, copyright 2018, Royal Society of Chemistry. (c) Comparison of selectivity of first protonation step of CO_2RR and the competitive HER. It shows that all the studied transition metals except for Co preferentially participate in the CO_2RR over the HER. Reproduced with permission from ref. 146, copyright 2018, Royal Society of Chemistry. (d) The free energy profile of the CO_2RR for the Mo-MOF electrocatalyst that shows preferable CH_4 production, while the formation of other products exhibit high energy barriers, as highlighted by the red lines. Reproduced with permission from ref. 145, copyright 2020, Elsevier. The last protonation step to produce H_2O is the RDS, which required a limiting potential of 0.42 eV.

Transition metals are regarded as promising candidates because of their many d-orbital electrons and the variation valence states. The electrochemical activity and selectivity of SACs toward the CO_2RR depends on the central metal atom and its coordination environment. More precisely, the activity is related to the electronic structure, which can be modulate through the coordination environment and valence states. In such a study, the CO_2RR performance of metal-doped nitrogen carbon based SACs was correlated with an intrinsic descriptor, based on the electronic states of the transition metals. The intrinsic descriptor Φ constitutes the number of valence electrons, the electronegativity of the transition metal and the radius of the transition metal.[19] The theoretical calculations predicted that Co-based SACs could achieve high electrochemical performance for the CO_2RR. Various products can be visualized for the electrochemical CO_2RR, but CO (as a simple one due to the two-electron transfer process) is used to access the electrochemical performance of the CO_2RR. CO formation is hindered by the weak adsorption of CO_2 and desorption of the CO from the active surface, which is limited by the strong adsorption of CO. In such a case, Ni atoms coordinated to a graphene support as an active site were shown to form an electronic structure that facilitates the CO formation in the CO_2RR while simultaneously hindering the HER.[134] In another investigation, TM–N_x–C moieties with double vacancies were thoroughly studied for the electrochemical reduction of CO_2 to CO. A scaling relationship was observed between the adsorption energy of *COOH and *CO to measure the CO_2RR activity for CO formation. According to thermodynamics analysis, Ni–N_1, Pd–N_1, Pt–N_1, Co–N_4, and Rh–N_4 are the most prominent active sites for the CO formation because these systems show moderate binding strength toward *COOH and *CO, which facilitates CO formation. While, Fe–N_4 was predicted to be more favorable for the further reduction of CO to CH_3OH and CH_4 at a relatively low electrode potential of between −0.7 and 0.9 V.[135] In another study, Co-doped graphene altered with pyridinic nitrogen atoms was studied for the conversion of CO_2 to HCOOH. The electrocatalytic performance and electronic structure of Co SACs anchored on monovacancy (Co–N_3) and divacancy (Co–N_4) structures were compared towards the CO_2RR. The theoretical results revealed that the Co atom supported by a monovacancy (Co–N_3) exhibits superior performance in terms of CO_2 activation and product selectivity. The conversion of CO_2 to *HCOO requires an energy barrier of 0.31 eV, indicating that this reaction can easily accelerate under ambient conditions, while the second hydrogenation step to form the required product requires an overpotential of 0.51 eV.[136]

Regular and planar carbon materials, besides graphene, as substrates of SACs are highly desired for DFT calculations. For instance, Wang and coworkers studied transition metals anchored on a C_2N monolayer for the CO_2RR and found that the N_6 moiety serves as an active site for CO_2 activation and then protonation to form different products.[137] It was predicted that C_2N-supported SACs are more selective for CO_2 reduction over the HER and that CO_2-to-*COOH conversion is the RDS. According to the DFT calculated free energies of each intermediate, Ti and Mn-based SACs favor methane production, while Fe, Co, Ni, and Ru show high selectivity toward methanol over a potential range of 0.5–0.8 eV, with the detailed pathways shown in Fig. 7b. In search of a more stable and conductive substrate, graphyne as a two-dimensional carbon planar materials with high stability and plasticity is a good candidate on which to stabilize single metal atoms. DFT was employed to assess the performance of SACs embedded in graphyne for the CO_2RR.[138] Based on reaction barriers, it was discovered that Cr–G was the most efficient catalyst for the CO_2RR, with the HER being suppressed during electrocatalysis. In the optimal pathway, the Cr–G catalyst most probably generates a final product of CH_4, and the RDS is *CH_3 to CH_4 conversion, which only requires a limiting potential of −0.29 eV.[138] Graphdiyne, a new 2D planar carbon allotrope, formed from sp–sp^2 hybridized carbon atoms, has received a huge amount of attention due to its unique characteristics and wide applications in catalysis and other fields.[139] In a theoretical study, the electrochemical performance of alkali metals supported on a graphdiyne substrate was evaluated for the reduction of CO_2 to HCOOH. The results indicate that the electrocatalysts exhibit excellent stability and can be realized experimentally. Among the studied alkali metals, Na and Li had the capacity to strongly adsorb CO_2 and activate it. Based on adsorption free energy, the binding between *OCHO and alkali metals is stronger than that between *COOH and alkali metals. This indicates that *HCCOH is preferentially formed *via* the CO_2RR, and Li@GDY required a limiting potential of −0.56 V, while Na@GDY required a lower overpotential of −0.16 V.[140] Fe anchored on graphdiyne has been shown to achieve high selectivity and activity in the CO_2RR towards CH_4 production. The reduction of CO to *COH is the rate determining step, which requires a limiting potential of −0.33 V.[141]

g-C_3N_4 has been used to reveal the mechanistic aspects of the CO_2RR by embedding it with a variety of transition metals.[142] Based on the adsorption energies of *CO and *H, a descriptor-based picture was built for the product distribution, where seven metals, Pt, Ru, Co, Ni, Pd, Fe, and Cu, were predicted to have the capacity to generate products toward C_2H_4. Notably, in terms of the rich vacancy/edge sites and N-atom contents of g-C_3N_4, the atomic model in the calculation was constructed as a unique M–N_6 structure, which may contribute toward the results that seven metal-based SACs generate materials beyond C_1 products.[142] A series of transition metals supported on graphitic carbon nitride have been investigated for the CO_2RR using DFT. Mn–C_3N was shown to be the most prominent electrocatalyst due to its high activity and selectivity toward HCOOH formation. The HER was successfully suppressed on this surface and required a very low overpotential of 0.04 V, while a kinetic energy barrier of 0.75 eV was required for the first protonation step.[143] While, in another study, TM-doped g-C_3N_4 was theoretically evaluated for the reduction of CO_2 to C_1 products, *i.e.* CH_3OH and CH_4. Ni/g-C_3N_4 tends to convert CO_2 to CH_3OH with a limiting potential of 0.72 V, while Fe/g-C_3N_4 and Co/g-C_3N_4 preferably produce CH_4 with limiting potentials of 0.67 and 0.81 V, respectively.[144] In an interesting study, a novel 2D MOF was utilized as a support for SACs for use in the

CO_2RR.[145] Among the studied transition metals, a Mo-based MOF was determined to be the most efficient electrocatalyst due to its performance during the adsorption and transformation of CO_2. The low energy barrier of 0.47 eV for Mo-SACs was even lower than that of a (211) Cu surface, and the proposed optimal mechanism on the Mo-SACs was *CO → *COOH → *HCOOH → *CHO → *CH_2O → *CH_2OH → *CH_3 → *CH_4, as shown in Fig. 7d.[145]

Adding metal atoms into coordination networks with unsaturated active sites that act as Lewis-acid sites can produce active materials. Phthalocyanine (Pc) has been predicted to be an efficient candidate due to its good binding energy toward independent metal atoms uniformly dispersed on a monolayer. As shown in Fig. 7c, a Pc monolayer was shown to support TM-SACs and it was found that most metals favored the first protonation step of the CO_2RR rather than the competitive HER.[146] Co–Pc was predicted to be the most efficient electrocatalyst for HCHO, with an overpotential of 0.36 V, while Cr, Mn, and Zn-based SACs were dominated by HCOOH products according to their calculated Gibbs free energies. Among all these studied metals, Mn–Pc exhibited the lowest overpotential of 0.017 V, while Fe–Pc showed the highest overpotential of 0.819 V toward the CO_2RR. In another case, coordinated multidentate ligands were shown to make structures flexible and ideal for applications. For instance, tetracyanoquinodimethane (TCNQ) was explored as a coordination molecule to be doped with various single metal atoms for the CO_2RR.[147] HCOOH was predicted to be the primary product for V, Cr, Mn, Ni and Cu-based SACs, while Co and Fe-based electrocatalysts favored four-electron transferred HCHO as the main product. The modification of the coordinated environment of the active metal center alters the d-electron configuration and is used to tune the adsorption energies of the reactants and reaction intermediates for better electrochemical performance. In such a DFT study, the effect of coordination engineering of a Co–N_4 porphyrin toward the CO_2RR was studied by replacing N with C or O.[148] By evaluating 24 different Co-centered coordination sites, the Co–O_3N_1 porphyrin was predicted to be the most efficient for the electrochemical conversion of CO_2 to CO. Detailed analysis of the electronic structure revealed that the lack of π-bonding in Co–O bonds compared to Co–N and Co–C bonds was responsible for the enhanced catalytic activity.[148] In another research study, N and S coordination effects were studied for the CO_2RR by comparing Fe–N_2S_2 with an Fe–N_4 porphyrin. The results indicated that the combination of N and S provides a more stable structure than N coordination alone. The addition of S atoms forms a non-coplanar porphyrin framework, and more electrons accumulate on the Fe–S bond, promoting more vital interaction between the Fe and S atoms. The additional d_{z^2} orbitals of Fe efficiently tune the adsorption of CO_2 and intermediates and accelerate the overall kinetics of the CO_2RR. The S addition in coordination effectively decreases the limiting potential, and the Fe–N_2S_2 electrocatalyst shows a limiting potential of −0.38 eV for CO_2 conversion to HCOOH.[149] A similar study revealed that Ni-SACs with two C, one N, and one S coordination environment were estimated to be the most efficient catalyst for the CO_2RR, with a theoretically calculated onset potential of 0.67 eV.[150]

5.2 Machine learning-accelerated design of SACs

DFT calculations have been extensively applied for the discovery and design of SACs for the CO_2RR through the prediction of their activity, stability, and structure sensitivity.[151,152] However, DFT calculations are time- and resource-consuming for the high-throughput screening of SACs in the vast parameter space. In this regard, machine learning (ML) as a strong and supportive tool can guide DFT calculations to accelerate and simplify the rational design of SACs *via* the establishment of accurate and deep structure–activity relationships coupled with feature importance analysis.[153–156] For example, neural network algorithms were developed to calculate the adsorption energies of CO* and the formation energies of HOCO* in order to identify the performances of surface sites on Au nanoparticles as well as de-alloyed Au surfaces for the CO_2RR.[157] Similarly, ML was applied to DFT-calculated data to discover active bimetallic facets for the CO_2RR and the results revealed that most facets of nickel gallium bimetallics lead to similar activity on Ni surfaces.[155] Moreover, structure–activity relationships were established for predicting CO and H adsorption energies based on structural properties using active learning across intermediates. In fact, an automated screening approach through integration and optimization of ML was presented to guide DFT calculations for predicting catalytic activity. The feasibility of this approach was demonstrated by screening various alloys combining 31 elements, which resulted in 131 candidate surfaces across 54 alloys being identified for the CO_2RR and the identification of 258 surfaces across 54 alloys for the CO_2RR.[158] Similarly, active learning was then used to accelerate the screening of CO adsorption energy on Cu-based components.[159] In addition, extreme gradient boosting regression (XGBR) was implemented as a supervised ML algorithm to screen ΔG_{CO*} and ΔG_{H*} of 1060 SACs embedded in metal-nonmetal co-doped graphene for the CO_2RR, as shown in the inset of Fig. 8a.[160] Based on feature importance analysis, the Pauling-electronegativity (E_M), covalent radius (M_cov), and first ionization energy of the SACs (1E_M) are the most important parameters on ΔG_{CO*} (Fig. 8a). Comparison of predicted values using the XGBR model and DFT calculations, shown in Fig. 8b, indicated that ML was able to accurately predict ΔG_{CO*}. Therefore, the XGBR model was used for the accelerated high-throughput screening of ΔG_{CO*} in the design of SACs, leading to a huge decrease in the number of DFT calculations, as depicted in Fig. 8c.[160] Additionally, atomic properties were used to predict the catalytic activity of SACs and dual-atom catalysts for the CO_2RR. Based on results from the XGBR algorithm, Ag–MoPc was revealed as an excellent electrocatalyst, with a limiting potential of −0.33 V.[161] Subsequently, the data from the abovementioned work was used as an example to evaluate the efficiency of a DFT–ML hybrid program for catalysis programming.[162] Obviously, ML has been successfully applied to accelerate the design and discovery of SACs for the CO_2RR. However, this technique is still in its infancy and there is thus a need for further optimization and development of materials simulations.

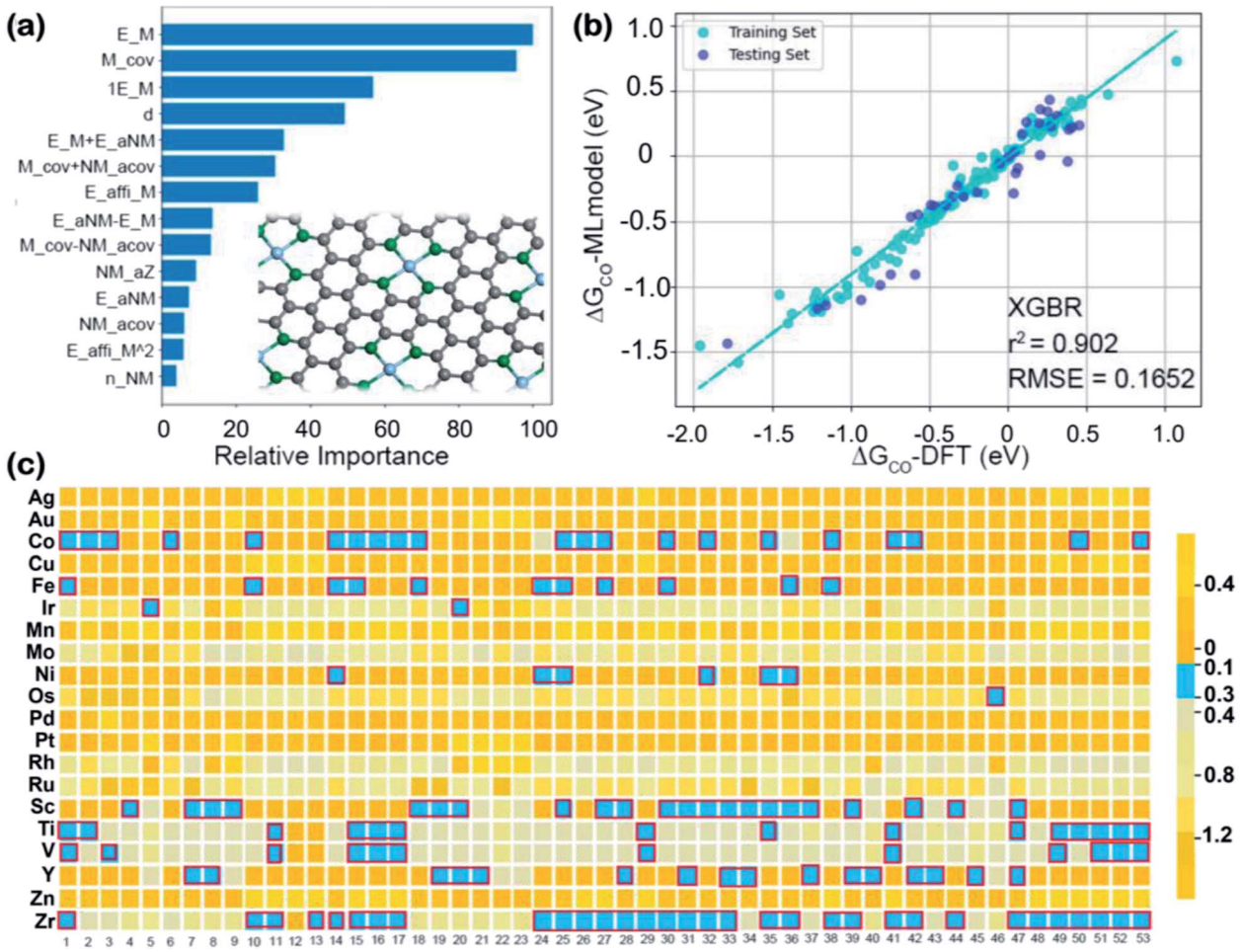

Fig. 8 Machine Learning for the CO_2RR. (a) Feature importance analysis for ΔG_{CO*} prediction using ML. Pauling electronegativity (E_M), covalent radius (M_cov), and first ionization energy of transition metal atoms as SACs (1E_M) are the most important parameters. The inset shows the structures of SACs used for the CO_2RR. Green, gray, and blue spheres indicate nonmetal, carbon, and transition metal atoms, respectively. (b) Comparison of ML- and DFT-predicted ΔG_{CO*}. (c) High-throughput screening of ΔG_{CO*} using XGBR models. Reproduced with permission from ref. 160, copyright 2020, American Chemical Society. These figures indicate that ML can accurately predict ΔG_{CO*} for the better design of SACs.

6. Summary and perspective

As discussed in this review, the fundamental knowledge for the CO_2RR on non-noble metal-based SACs on 2D substrates is introduced based on recent studies. The decisive factors for efficient CO_2 transformation, including central metal selection, metal valence regulation, SAC loading and distribution, cell configurations, electrolytes, *etc.* were discussed and Cu-based SACs for C_2/C_{2+} products were emphasized. The proposed atomic structures of the active sites on carbon-based materials that can be used to intuitively compare mechanistic investigations between various studies and the rational design of optimum catalytic sites were systematically summarized. In addition, the application of state-of-art spectroscopies, especially *in situ* or *operando* techniques, in CO_2RR studies presents an exciting approach to gain insights from structure–activity relationships. Furthermore, computational inspiration of the novel theoretical understanding of the catalytic mechanisms and ML as a rising research direction toward accelerating catalyst screening by integrating DFT calculations were discussed.

Despite the fast development in SAC designs and mechanism studies laying the foundation for future research on the CO_2RR, there are still multiple challenges that remain in the field:

(1) Rational designs of electrodes and electrolyzers that enable the CO_2RR to be endured at a high current density and relatively large applied potential. To date, a few studies have reported the large-scale preparation of SACs and measured their CO_2RR performance in flow cell or MEA-cell electrolyzers.[62,65,163] It shows great promise for future that researchers can start with these prototypes and subsequently expand SACs to an industrial scale. Accordingly, the exploration of scalable SACs, robust electrodes that can integrate SACs readily, electrolyzer configuration and even electrolytes are further needed.

(2) Enriching the designs of SACs with reduced CO_2RR products. An isolated active site is difficult to afford C–C coupling, not to mention the restrictions on metal selection.

Many existing reports have achieved nearly 100% CO_2-to-CO conversion on nonprecious SACs but hardly reduced CO_2 to C_2/C_{2+} products. Hence, fabricating diatom or even multi-atom-based SACs is highly encouraged.[90] As tunable adsorption and desorption energies can be realized on neighboring dual metal atoms, there are new opportunities to promote C–C coupling and find optimal metal pairs for obtaining target products.

(3) Proper monitoring of the dynamic structural evolution of active sites. Further development of spectroscopic and microscopic techniques, especially *in situ*/*operando* techniques, to offer more real-time information during electrocatalysis is significant to identify the geometric and electronic structures of the real active moieties and make molecular models more plausible.

(4) Although remarkable progress has been made in developing SACs, product selectivity, energy efficiency, reaction kinetics, and electrocatalyst stability under harsh conditions are still challenging for practical realization. Theoretical calculations play an essential role in predicting the active catalysts, reaction mechanism, and electronic structure of the active site to understand the catalyst activity. However, only a few mechanistic studies based on DFT calculations on SACs are available regarding product selectivity and reaction kinetics. Usually, the reaction conditions are ignored in predicting prominent electrocatalysts and free energy profiles *via* DFT calculations. Therefore, to gain fundamental insights into the reaction energies and product selectivity, it is highly desirable to include environmental factors such as solvation effects (implicit or explicit), pH, and electric field in DFT calculations.

(5) ML in combination with DFT has been recently implemented in the design and discovery of SACs for the CO_2RR. The accuracy and predictive power depends strongly on the input features, ML algorithms, and the quality as well as size of training and test database.[29] Therefore, more studies and efforts are still required to use universal descriptors as input features, use a general ML algorithm, and increase the input database.[164] Moreover, the descriptors obtained from ML can be helpful for constructing volcano plots to understand the origin of SAC activity. However, due to the diversity of reaction intermediates, the complexity of the CO_2RR, and lack of appropriate descriptors as input features to accelerate the rational design of SACs, the application of ML algorithms in the reaction mechanism of the CO_2RR is still in its early stage.[91,165] Active ML is also highly desired for the future investigation of catalytic activity, metal–support interactions, and manipulation of the coordination structure of highly selective and stable SACs.

Overall, mechanistic understanding from the integration of experimental and computational insights can help to guide the design of SACs toward high activity and selectivity. We believe a more thorough investigation of nonprecious metal-based SACs for the CO_2RR will be achieved in the future.

Author contributions

Y. H., F. R. and M. T. participated in the organization, writing and editing of this manuscript. X. L., Y. Q. H., T. Z. and Z. L. inspired this review and assisted in the editorial process.

Conflicts of interest

The authors declare no competing interests.

Acknowledgements

Z. L. acknowledges support from the NSFC-RGC Joint Research Scheme (N_HKUST607/17), the IER foundation (HT-JD-CXY-201907), the "International science and technology cooperation projects" of the Science and Technological Bureau of Guangzhou Huangpu District (2019GH06), the Guangdong Science and Technology Department (Project#: 2020A0505090003), and the Research Fund of Guangdong-Hong Kong-Macao Joint Laboratory for Intelligent Micro-Nano Optoelectronic Technology (No. 2020B1212030010).

References

1 S. Chu, Y. Cui and N. Liu, *Nat. Mater.*, 2016, **16**, 16–22.
2 E. V. Kondratenko, G. Mul, J. Baltrusaitis, G. O. Larrazábal and J. Pérez-Ramírez, *Energy Environ. Sci.*, 2013, **6**, 3112–3135.
3 Z. Yang, J. Zhang, M. C. Kintner-Meyer, X. Lu, D. Choi, J. P. Lemmon and J. Liu, *Chem. Rev.*, 2011, **111**, 3577–3613.
4 WMO, *Greenhouse Gas Concentrations in the Atmosphere WMO-Global Atmosphere Watch*, 2021, https://library.wmo.int/doc_num.php?explnum_id=10794.
5 A. Majumdar and J. Deutch, *Joule*, 2018, **2**, 805–809.
6 D. Wakerley, S. Lamaison, F. Ozanam, N. Menguy, D. Mercier, P. Marcus, M. Fontecave and V. Mougel, *Nat. Mater.*, 2019, **18**, 1222–1227.
7 X. Li, J. Lin, L. Li, Y. Huang, X. Pan, S. E. Collins, Y. Ren, Y. Su, L. Kang and X. Liu, *Angew. Chem., Int. Ed.*, 2020, **59**, 19983–19989.
8 J. E. Huang, F. Li, A. Ozden, A. S. Rasouli, F. P. G. de Arquer, S. Liu, S. Zhang, M. Luo, X. Wang and Y. Lum, *Science*, 2021, **372**, 1074–1078.
9 L. Zhang, Z. Wei, S. Thanneeru, M. Meng, M. Kruzyk, G. Ung, B. Liu and J. He, *Angew. Chem., Int. Ed.*, 2019, **58**, 15834–15840.
10 S. Nitopi, E. Bertheussen, S. B. Scott, X. Liu, A. K. Engstfeld, S. Horch, B. Seger, I. E. L. Stephens, K. Chan, C. Hahn, J. K. Norskov, T. F. Jaramillo and I. Chorkendorff, *Chem. Rev.*, 2019, **119**, 7610–7672.
11 C. G. Morales-Guio, E. R. Cave, S. A. Nitopi, J. T. Feaster, L. Wang, K. P. Kuhl, A. Jackson, N. C. Johnson, D. N. Abram, T. Hatsukade, C. Hahn and T. F. Jaramillo, *Nat. Catal.*, 2018, **1**, 764–771.
12 R. Francke, B. Schille and M. Roemelt, *Chem. Rev.*, 2018, **118**, 4631–4701.
13 L. Wang, W. Chen, D. Zhang, Y. Du, R. Amal, S. Qiao, J. Wu and Z. Yin, *Chem. Soc. Rev.*, 2019, **48**, 5310–5349.
14 K. P. Kuhl, E. R. Cave, D. N. Abram and T. F. Jaramillo, *Energy Environ. Sci.*, 2012, **5**, 7050–7059.
15 J. T. Feaster, C. Shi, E. R. Cave, T. Hatsukade, D. N. Abram, K. P. Kuhl, C. Hahn, J. K. Nørskov and T. F. Jaramillo, *ACS Catal.*, 2017, **7**, 4822–4827.

16 J. J. Leung, J. A. Vigil, J. Warnan, E. Edwardes Moore and E. Reisner, *Angew. Chem., Int. Ed.*, 2019, **58**, 7697–7701.
17 B. Qiao, A. Wang, X. Yang, L. F. Allard, Z. Jiang, Y. Cui, J. Liu, J. Li and T. Zhang, *Nat. Chem.*, 2011, **3**, 634–641.
18 X.-F. Yang, A. Wang, B. Qiao, J. Li, J. Liu and T. Zhang, *Acc. Chem. Res.*, 2013, **46**, 1740–1748.
19 L. Gong, D. Zhang, C. Y. Lin, Y. Zhu, Y. Shen, J. Zhang, X. Han, L. Zhang and Z. Xia, *Adv. Energy Mater.*, 2019, **9**, 1902625.
20 S. Tian, M. Hu, Q. Xu, W. Gong, W. Chen, J. Yang, Y. Zhu, C. Chen, J. He and Q. Liu, *Sci. China Mater.*, 2021, **64**, 642–650.
21 J. Mao, C.-T. He, J. Pei, Y. Liu, J. Li, W. Chen, D. He, D. Wang and Y. Li, *Nano Lett.*, 2020, **20**, 3442–3448.
22 S. Back, J. Lim, N. Y. Kim, Y. H. Kim and Y. Jung, *Chem. Sci.*, 2017, **8**, 1090–1096.
23 K. Jiang, S. Siahrostami, T. Zheng, Y. Hu, S. Hwang, E. Stavitski, Y. Peng, J. Dynes, M. Gangisetty, D. Su, K. Attenkofer and H. Wang, *Energy Environ. Sci.*, 2018, **11**, 893–903.
24 T. Sheng and S.-G. Sun, *Chem. Phys. Lett.*, 2017, **688**, 37–42.
25 X. Song, H. Zhang, Y. Yang, B. Zhang, M. Zuo, X. Cao, J. Sun, C. Lin, X. Li and Z. Jiang, *Adv. Sci.*, 2018, **5**, 1800177.
26 C. Xu, A. Vasileff, Y. Zheng and S. Z. Qiao, *Adv. Mater. Interfaces*, 2020, **8**, 2001904.
27 M. Jia, Q. Fan, S. Liu, J. Qiu and Z. Sun, *Curr. Opin. Green Sustain.*, 2019, **16**, 1–6.
28 T. Wang, Q. Zhao, Y. Fu, C. Lei, B. Yang, Z. Li, L. Lei, G. Wu and Y. Hou, *Small Methods*, 2019, **3**, 1900210.
29 S. Zhu, E. P. Delmo, T. Li, X. Qin, J. Tian, L. Zhang and M. Shao, *Adv. Mater.*, 2021, e2005484, DOI: 10.1002/adma.202005484.
30 X. Li, X. Yang, Y. Huang, T. Zhang and B. Liu, *Adv. Mater.*, 2019, **31**, 1902031.
31 Y. Cheng, S. Zhao, B. Johannessen, J. P. Veder, M. Saunders, M. R. Rowles, M. Cheng, C. Liu, M. F. Chisholm and R. De Marco, *Adv. Mater.*, 2018, **30**, 1706287.
32 C. Lu, J. Yang, S. Wei, S. Bi, Y. Xia, M. Chen, Y. Hou, M. Qiu, C. Yuan, Y. Su, F. Zhang, H. Liang and X. Zhuang, *Adv. Funct. Mater.*, 2019, **29**, 1806884.
33 A. Bagger, W. Ju, A. S. Varela, P. Strasser and J. Rossmeisl, *ChemPhysChem*, 2017, **18**, 3266–3273.
34 L. Fan, C. Xia, F. Yang, J. Wang, H. Wang and Y. Lu, *Sci. Adv.*, 2020, **6**, eaay3111.
35 P. P. Yang, X. L. Zhang, F. Y. Gao, Y. R. Zheng, Z. Z. Niu, X. Yu, R. Liu, Z. Z. Wu, S. Qin, L. P. Chi, Y. Duan, T. Ma, X. S. Zheng, J. F. Zhu, H. J. Wang, M. R. Gao and S. H. Yu, *J. Am. Chem. Soc.*, 2020, **142**, 6400–6408.
36 R. Kortlever, J. Shen, K. J. P. Schouten, F. Calle-Vallejo and M. T. Koper, *J. Phys. Chem. Lett.*, 2015, **6**, 4073–4082.
37 A. D. Handoko, F. Wei, Jenndy, B. S. Yeo and Z. W. Seh, *Nat. Catal.*, 2018, **1**, 922–934.
38 S. Chen, H. Yuan, S. I. Morozov, L. Ge, L. Li, L. Xu and W. A. Goddard III, *J. Phys. Chem. Lett.*, 2020, **11**, 2541–2549.
39 M. G. Kibria, J. P. Edwards, C. M. Gabardo, C. T. Dinh, A. Seifitokaldani, D. Sinton and E. H. Sargent, *Adv. Mater.*, 2019, **31**, 1807166.
40 P. De Luna, R. Quintero-Bermudez, C.-T. Dinh, M. B. Ross, O. S. Bushuyev, P. Todorović, T. Regier, S. O. Kelley, P. Yang and E. H. Sargent, *Nat. Catal.*, 2018, **1**, 103–110.
41 S. G. Han, D. D. Ma and Q. L. Zhu, *Small Methods*, 2021, **5**, 2100102.
42 A. Vasileff, C. Xu, Y. Jiao, Y. Zheng and S.-Z. Qiao, *Chem*, 2018, **4**, 1809–1831.
43 Z. Wang, J. Zhao and Q. Cai, *Phys. Chem. Chem. Phys.*, 2017, **19**, 23113–23121.
44 A. Bagger, W. Ju, A. S. Varela, P. Strasser and J. Rossmeisl, *Catal. Today*, 2017, **288**, 74–78.
45 M. Li, H. Wang, W. Luo, P. C. Sherrell, J. Chen and J. Yang, *Adv. Mater.*, 2020, **32**, e2001848.
46 W. Ju, A. Bagger, G. P. Hao, A. S. Varela, I. Sinev, V. Bon, B. Roldan Cuenya, S. Kaskel, J. Rossmeisl and P. Strasser, *Nat. Commun.*, 2017, **8**, 1–9.
47 J. Li, P. Pršlja, T. Shinagawa, A. J. Martin Fernandez, F. Krumeich, K. Artyushkova, P. Atanassov, A. Zitolo, Y. Zhou and R. García-Muelas, *ACS Catal.*, 2019, **9**, 10426–10439.
48 Q. Fan, P. Hou, C. Choi, T. S. Wu, S. Hong, F. Li, Y. L. Soo, P. Kang, Y. Jung and Z. Sun, *Adv. Energy Mater.*, 2019, **10**, 1903068.
49 R. Sun, Y. Liao, S.-T. Bai, M. Zheng, C. Zhou, T. Zhang and B. F. Sels, *Energy Environ. Sci.*, 2021, **14**, 1247–1285.
50 S. Back and Y. Jung, *ACS Energy Lett.*, 2017, **2**, 969–975.
51 S. Zhao, G. Chen, G. Zhou, L. C. Yin, J. P. Veder, B. Johannessen, M. Saunders, S. Z. Yang, R. De Marco, C. Liu and S. P. Jiang, *Adv. Funct. Mater.*, 2019, **30**, 1906157.
52 C. Gao, S. Chen, Y. Wang, J. Wang, X. Zheng, J. Zhu, L. Song, W. Zhang and Y. Xiong, *Adv. Mater.*, 2018, **30**, 1704624.
53 S.-G. Han, D.-D. Ma, S.-H. Zhou, K. Zhang, W.-B. Wei, Y. Du, X.-T. Wu, Q. Xu, R. Zou and Q.-L. Zhu, *Appl. Catal. B*, 2021, **283**, 119591.
54 Y. Qu, Z. Li, W. Chen, Y. Lin, T. Yuan, Z. Yang, C. Zhao, J. Wang, C. Zhao, X. Wang, F. Zhou, Z. Zhuang, Y. Wu and Y. Li, *Nat. Catal.*, 2018, **1**, 781–786.
55 L. Jiao, R. Zhang, G. Wan, W. Yang, X. Wan, H. Zhou, J. Shui, S. H. Yu and H. L. Jiang, *Nat. Commun.*, 2020, **11**, 1–7.
56 H. J. Zhu, M. Lu, Y. R. Wang, S. J. Yao, M. Zhang, Y. H. Kan, J. Liu, Y. Chen, S. L. Li and Y. Q. Lan, *Nat. Commun.*, 2020, **11**, 1–10.
57 Q. Cao, L.-L. Zhang, C. Zhou, J.-H. He, A. Marcomini and J.-M. Lu, *Appl. Catal. B*, 2021, **294**, 120238.
58 L. Zou, Y. S. Wei, C. C. Hou, C. Li and Q. Xu, *Small*, 2021, **17**, e2004809.
59 K. Huang, J.-Y. Zhang, F. Liu and S. Dai, *ACS Catal.*, 2018, **8**, 9079–9102.
60 S. B. Peh and D. Zhao, *Science*, 2020, **369**, 372–373.
61 Q. Wu, M. J. Mao, Q. J. Wu, J. Liang, Y. B. Huang and R. Cao, *Small*, 2021, **17**, 2004933.
62 C. Xia, Y. Qiu, Y. Xia, P. Zhu, G. King, X. Zhang, Z. Wu, J. Y. T. Kim, D. A. Cullen, D. Zheng, P. Li, M. Shakouri, E. Heredia, P. Cui, H. N. Alshareef, Y. Hu and H. Wang, *Nat. Chem.*, 2021, **13**, 887–894.

63 M. R. Singh, E. L. Clark and A. T. Bell, *Phys. Chem. Chem. Phys.*, 2015, **17**, 18924–18936.
64 D. Higgins, C. Hahn, C. Xiang, T. F. Jaramillo and A. Z. Weber, *ACS Energy Lett.*, 2018, **4**, 317–324.
65 Z. Chen, X. Zhang, W. Liu, M. Jiao, K. Mou, X. Zhang and L. Liu, *Energy Environ. Sci.*, 2021, **14**, 2349–2356.
66 H. Jiang, L. Wang, B. Gao, Y. Li, Y. Guo, M. Zhuo, K. Sun, B. Lu, M. Jia, X. Yu, H. Wang and Y. Li, *Chem. Eng. J.*, 2021, **422**, 129923.
67 D. Gao, R. M. Arán-Ais, H. S. Jeon and B. Roldan Cuenya, *Nat. Catal.*, 2019, **2**, 198–210.
68 T. Zheng, K. Jiang and H. Wang, *Adv. Mater.*, 2018, **30**, 1802066.
69 D. Karapinar, N. T. Huan, N. Ranjbar Sahraie, J. Li, D. Wakerley, N. Touati, S. Zanna, D. Taverna, L. H. Galvão Tizei and A. Zitolo, *Angew. Chem., Int. Ed.*, 2019, **58**, 15098–15103.
70 E. Boutin, M. Wang, J. C. Lin, M. Mesnage, D. Mendoza, B. Lassalle-Kaiser, C. Hahn, T. F. Jaramillo and M. Robert, *Angew. Chem., Int. Ed.*, 2019, **58**, 16172–16176.
71 Y. Wu, Z. Jiang, X. Lu, Y. Liang and H. Wang, *Nature*, 2019, **575**, 639–642.
72 H. Yang, Y. Wu, G. Li, Q. Lin, Q. Hu, Q. Zhang, J. Liu and C. He, *J. Am. Chem. Soc.*, 2019, **141**, 12717–12723.
73 A. Guan, Z. Chen, Y. Quan, C. Peng, Z. Wang, T.-K. Sham, C. Yang, Y. Ji, L. Qian, X. Xu and G. Zheng, *ACS Energy Lett.*, 2020, **5**, 1044–1053.
74 J. Zhao, J. Zhao, F. Li and Z. Chen, *J. Phys. Chem. C*, 2018, **122**, 19712–19721.
75 K. Zhao, X. Nie, H. Wang, S. Chen, X. Quan, H. Yu, W. Choi, G. Zhang, B. Kim and J. G. Chen, *Nat. Commun.*, 2020, **11**, 1–10.
76 T. Zhang, X. Han, H. Yang, A. Han, E. Hu, Y. Li, X. q. Yang, L. Wang, J. Liu and B. Liu, *Angew. Chem., Int. Ed.*, 2020, **132**, 12153–12159.
77 J. Gu, C.-S. Hsu, L. Bai, H. M. Chen and X. Hu, *Science*, 2019, **364**, 1091–1094.
78 X. Li, Y. Zeng, C.-W. Tung, Y.-R. Lu, S. Baskaran, S.-F. Hung, S. Wang, C.-Q. Xu, J. Wang, T.-S. Chan, H. M. Chen, J. Jiang, Q. Yu, Y. Huang, J. Li, T. Zhang and B. Liu, *ACS Catal.*, 2021, **11**, 7292–7301.
79 A. Wang, J. Li and T. Zhang, *Nat. Rev. Chem.*, 2018, **2**, 65–81.
80 X. Wang, Z. Chen, X. Zhao, T. Yao, W. Chen, R. You, C. Zhao, G. Wu, J. Wang, W. Huang, J. Yang, X. Hong, S. Wei, Y. Wu and Y. Li, *Angew. Chem., Int. Ed.*, 2018, **57**, 1944–1948.
81 J. Yang, Z. Qiu, C. Zhao, W. Wei, W. Chen, Z. Li, Y. Qu, J. Dong, J. Luo, Z. Li and Y. Wu, *Angew. Chem., Int. Ed.*, 2018, **57**, 14095–14100.
82 S. Feng, W. Zheng, J. Zhu, Z. Li, B. Yang, Z. Wen, J. Lu, L. Lei, S. Wang and Y. Hou, *Appl. Catal. B.*, 2020, 270.
83 X. Zhang, Y. Wang, M. Gu, M. Wang, Z. Zhang, W. Pan, Z. Jiang, H. Zheng, M. Lucero, H. Wang, G. E. Sterbinsky, Q. Ma, Y.-G. Wang, Z. Feng, J. Li, H. Dai and Y. Liang, *Nat. Energy*, 2020, **5**, 684–692.
84 S. Tian, Q. Fu, W. Chen, Q. Feng, Z. Chen, J. Zhang, W.-C. Cheong, R. Yu, L. Gu and J. Dong, *Nat. Commun.*, 2018, **9**, 1–7.
85 J. Mahmood, F. Li, S. M. Jung, M. S. Okyay, I. Ahmad, S. J. Kim, N. Park, H. Y. Jeong and J. B. Baek, *Nat. Nanotechnol.*, 2017, **12**, 441–446.
86 X. Zhao and Y. Liu, *J. Am. Chem. Soc.*, 2020, **142**, 5773–5777.
87 C. Yan, H. Li, Y. Ye, H. Wu, F. Cai, R. Si, J. Xiao, S. Miao, S. Xie, F. Yang, Y. Li, G. Wang and X. Bao, *Energy Environ. Sci.*, 2018, **11**, 1204–1210.
88 W. Zheng, J. Yang, H. Chen, Y. Hou, Q. Wang, M. Gu, F. He, Y. Xia, Z. Xia, Z. Li, B. Yang, L. Lei, C. Yuan, Q. He, M. Qiu and X. Feng, *Adv. Funct. Mater.*, 2019, **30**, 1907658.
89 J. Feng, H. Gao, L. Zheng, Z. Chen, S. Zeng, C. Jiang, H. Dong, L. Liu, S. Zhang and X. Zhang, *Nat. Commun.*, 2020, **11**, 4341.
90 Q. Qu, S. Ji, Y. Chen, D. Wang and Y. Li, *Chem. Sci.*, 2021, **12**, 4201–4215.
91 M. D. Hossain, Y. Huang, T. H. Yu, W. A. Goddard III and Z. Luo, *Nat. Commun.*, 2020, **11**, 2256.
92 Z. Geng, Y. Cao, W. Chen, X. Kong, Y. Liu, T. Yao and Y. Lin, *Appl. Catal. B*, 2019, **240**, 234–240.
93 H. Zhang, J. Li, S. Xi, Y. Du, X. Hai, J. Wang, H. Xu, G. Wu, J. Zhang, J. Lu and J. Wang, *Angew. Chem., Int. Ed.*, 2019, **58**, 14871–14876.
94 Y. Pan, R. Lin, Y. Chen, S. Liu, W. Zhu, X. Cao, W. Chen, K. Wu, W. C. Cheong, Y. Wang, L. Zheng, J. Luo, Y. Lin, Y. Liu, C. Liu, J. Li, Q. Lu, X. Chen, D. Wang, Q. Peng, C. Chen and Y. Li, *J. Am. Chem. Soc.*, 2018, **140**, 4218–4221.
95 E. Jung, H. Shin, B.-H. Lee, V. Efremov, S. Lee, H. S. Lee, J. Kim, W. H. Antink, S. Park and K.-S. Lee, *Nat. mater.*, 2020, **19**, 436–442.
96 Y. Cai, J. Fu, Y. Zhou, Y. C. Chang, Q. Min, J. J. Zhu, Y. Lin and W. Zhu, *Nat. Commun.*, 2021, **12**, 1–9.
97 H. Kim, D. Shin, W. Yang, D. H. Won, H. S. Oh, M. W. Chung, D. Jeong, S. H. Kim, K. H. Chae, J. Y. Ryu, J. Lee, S. J. Cho, J. Seo, H. Kim and C. H. Choi, *J. Am. Chem. Soc.*, 2021, **143**, 925–933.
98 S. Cao, S. Wei, X. Wei, S. Zhou, H. Chen, Y. Hu, Z. Wang, S. Liu, W. Guo and X. Lu, *Small*, 2021, **17**, e2100949.
99 Y. Chen, R. Gao, S. Ji, H. Li, K. Tang, P. Jiang, H. Hu, Z. Zhang, H. Hao, Q. Qu, X. Liang, W. Chen, J. Dong, D. Wang and Y. Li, *Angew. Chem., Int. Ed.*, 2021, **60**, 3212–3221.
100 Y. Wu, C. Chen, X. Yan, X. Sun, Q. Zhu, P. Li, Y. Li, S. Liu, J. Ma, Y. Huang and B. Han, *Angew. Chem., Int. Ed.*, 2021, **113**, 20971–20978.
101 J. Wang, X. Huang, S. Xi, H. Xu and X. Wang, *Angew. Chem., Int. Ed.*, 2020, **59**, 19162–19167.
102 X. Wang, Y. Pan, H. Ning, H. Wang, D. Guo, W. Wang, Z. Yang, Q. Zhao, B. Zhang, L. Zheng, J. Zhang and M. Wu, *Appl. Catal. B*, 2020, **266**, 118630.
103 K. Mou, Z. Chen, X. Zhang, M. Jiao, X. Zhang, X. Ge, W. Zhang and L. Liu, *Small*, 2019, **15**, e1903668.
104 X. Rong, H. J. Wang, X. L. Lu, R. Si and T. B. Lu, *Angew. Chem., Int. Ed.*, 2020, **59**, 1961–1965.

105 X. Wang, S. Ding, T. Yue, Y. Zhu, M. Fang, X. Li, G. Xiao, Y. Zhu and L. Dai, *Nano Energy*, 2021, **82**, 105689.
106 C. Peng, G. Luo, J. Zhang, M. Chen, Z. Wang, T. K. Sham, L. Zhang, Y. Li and G. Zheng, *Nat. Commun.*, 2021, **12**, 1580.
107 F. Pan, H. Zhang, Z. Liu, D. Cullen, K. Liu, K. More, G. Wu, G. Wang and Y. Li, *J. Mater. Chem. A*, 2019, **7**, 26231–26237.
108 Y. Cheng, S. Zhao, H. Li, S. He, J.-P. Veder, B. Johannessen, J. Xiao, S. Lu, J. Pan, M. F. Chisholm, S.-Z. Yang, C. Liu, J. G. Chen and S. P. Jiang, *Appl. Catal. B*, 2019, **243**, 294–303.
109 Z. Zhang, J. Xiao, X. J. Chen, S. Yu, L. Yu, R. Si, Y. Wang, S. Wang, X. Meng and Y. Wang, *Angew. Chem., Int. Ed.*, 2018, **57**, 16339–16342.
110 W. Ju, A. Bagger, G.-P. Hao, A. S. Varela, I. Sinev, V. Bon, B. R. Cuenya, S. Kaskel, J. Rossmeisl and P. Strasser, *Nat. Commun.*, 2017, **8**, 1–9.
111 W. Xie, H. Li, G. Cui, J. Li, Y. Song, S. Li, X. Zhang, J. Y. Lee, M. Shao and M. Wei, *Angew. Chem., Int. Ed.*, 2021, **60**, 7382–7388.
112 Q. He, D. Liu, J. H. Lee, Y. Liu, Z. Xie, S. Hwang, S. Kattel, L. Song and J. G. Chen, *Angew. Chem., Int. Ed.*, 2020, **59**, 3033–3037.
113 X. Yang, T. Tat, A. Libanori, J. Cheng, X. Xuan, N. Liu, X. Yang, J. Zhou, A. Nashalian and J. Chen, *Mater. Today*, 2021, **45**, 54–61.
114 G. Luo, Y. Jing and Y. Li, *J. Mater. Chem. A*, 2020, **8**, 15809–15815.
115 M. Feng, X. Wu, H. Cheng, Z. Fan, X. Li, F. Cui, S. Fan, Y. Dai, G. Lei and G. He, *J. Mater. Chem. A*, 2021, **9**, 23817–23827.
116 W. Ren, X. Tan, W. Yang, C. Jia, S. Xu, K. Wang, S. C. Smith and C. Zhao, *Angew. Chem., Int. Ed.*, 2019, **58**, 6972–6976.
117 Y. Li, B. Wei, M. Zhu, J. Chen, Q. Jiang, B. Yang, Y. Hou, L. Lei, Z. Li, R. Zhang and Y. Lu, *Adv. Mater.*, 2021, **33**, 2102212.
118 Z. Zeng, L. Y. Gan, H. Bin Yang, X. Su, J. Gao, W. Liu, H. Matsumoto, J. Gong, J. Zhang, W. Cai, Z. Zhang, Y. Yan, B. Liu and P. Chen, *Nat. Commun.*, 2021, **12**, 4088.
119 W. Zhu, L. Zhang, S. Liu, A. Li, X. Yuan, C. Hu, G. Zhang, W. Deng, K. Zang, J. Luo, Y. Zhu, M. Gu, Z. J. Zhao and J. Gong, *Angew. Chem., Int. Ed.*, 2020, **59**, 12664–12668.
120 L. Lin, T. Liu, J. Xiao, H. Li, P. Wei, D. Gao, B. Nan, R. Si, G. Wang and X. Bao, *Angew. Chem., Int. Ed.*, 2020, **59**, 22408–22413.
121 E. J. Askins, M. R. Zoric, M. Li, Z. Luo, K. Amine and K. D. Glusac, *Nat. Commun.*, 2021, **12**, 3288.
122 A. Roe, D. Schneider, R. Mayer, J. Pyrz, J. Widom and L. Que Jr, *J. Am. Chem. Soc.*, 1984, **106**, 1676–1681.
123 L. Fang, S. Seifert, R. E. Winans and T. Li, *Small Methods*, 2021, **5**, 2001194.
124 Z. Jiang, T. Wang, J. Pei, H. Shang, D. Zhou, H. Li, J. Dong, Y. Wang, R. Cao and Z. Zhuang, *Energy Environ. Sci.*, 2020, **13**, 2856–2863.
125 P. Chen, N. Zhang, S. Wang, T. Zhou, Y. Tong, C. Ao, W. Yan, L. Zhang, W. Chu and C. Wu, *Proc. Natl. Acad. Sci. U.S.A.*, 2019, **116**, 6635–6640.
126 J. Timoshenko and A. Kuzmin, *Comput. Phys. Commun.*, 2009, **180**, 920–925.
127 S. Chen, Y. Li, Z. Bu, F. Yang, J. Luo, Q. An, Z. Zeng, J. Wang and S. Deng, *J. Mater. Chem. A*, 2021, **9**, 1705–1712.
128 Z. Weng, Y. Wu, M. Wang, J. Jiang, K. Yang, S. Huo, X. F. Wang, Q. Ma, G. W. Brudvig, V. S. Batista, Y. Liang, Z. Feng and H. Wang, *Nat. Commun.*, 2018, **9**, 415.
129 J. Li and J. Gong, *Energy Environ. Sci.*, 2020, **13**, 3748–3779.
130 S. Liu, H. B. Yang, S. F. Hung, J. Ding, W. Cai, L. Liu, J. Gao, X. Li, X. Ren, Z. Kuang, Y. Huang, T. Zhang and B. Liu, *Angew. Chem., Int. Ed.*, 2020, **59**, 798–803.
131 T. N. Huan, N. Ranjbar, G. Rousse, M. Sougrati, A. Zitolo, V. Mougel, F. Jaouen and M. Fontecave, *ACS Catal.*, 2017, **7**, 1520–1525.
132 S. Back, J. Lim, N.-Y. Kim, Y.-H. Kim and Y. Jung, *Chem. Sci.*, 2017, **8**, 1090–1096.
133 H. He and Y. Jagvaral, *Phys. Chem. Chem. Phys.*, 2017, **19**, 11436–11446.
134 K. Jiang, S. Siahrostami, T. Zheng, Y. Hu, S. Hwang, E. Stavitski, Y. Peng, J. Dynes, M. Gangisetty and D. Su, *Energy Environ. Sci.*, 2018, **11**, 893–903.
135 C. Guo, T. Zhang, X. Liang, X. Deng, W. Guo, Z. Wang, X. Lu and C.-M. L. Wu, *Appl. Surf. Sci.*, 2020, **533**, 147466.
136 M. D. Esrafili and B. Nejadebrahimi, *Appl. Surf. Sci.*, 2019, **475**, 363–371.
137 X. Cui, W. An, X. Liu, H. Wang, Y. Men and J. Wang, *Nanoscale*, 2018, **10**, 15262–15272.
138 L. Fu, R. Wang, C. Zhao, J. Huo, C. He, K.-H. Kim and W. Zhang, *Chem. Eng. J.*, 2021, **414**, 128857.
139 X. Gao, H. Liu, D. Wang and J. Zhang, *Chem. Soc. Rev.*, 2019, **48**, 908–936.
140 Z. Feng, G. Su, H. Ding, Y. Ma, Y. Li, Y. Tang and X. Dai, *Mol. Catal.*, 2020, **494**, 111142.
141 T. He, L. Zhang, G. Kour and A. Du, *J. CO_2 Util.*, 2020, **37**, 272–277.
142 S. Fu, X. Liu, J. Ran and Y. Jiao, *Catal. Today*, 2021, DOI: 10.1016/j.cattod.2021.06.013.
143 Y. Meng, Y. Gao, K. Li, H. Tang, Y. Wang and Z. Wu, *Appl. Surf. Sci.*, 2021, **542**, 148568.
144 C. Ao, B. Feng, S. Qian, L. Wang, W. Zhao, Y. Zhai and L. Zhang, *J. CO_2 Util.*, 2020, **36**, 116–123.
145 Q. Cui, G. Qin, W. Wang, K. Geethalakshmi, A. Du and Q. Sun, *Appl. Surf. Sci.*, 2020, **500**, 143993.
146 J.-H. Liu, L.-M. Yang and E. Ganz, *ACS Sustain. Chem. Eng.*, 2018, **6**, 15494–15502.
147 J.-H. Liu, L.-M. Yang and E. Ganz, *J. Mater. Chem. A*, 2019, **7**, 3805–3814.
148 H. Zhou, X. Zou, X. Wu, X. Yang and J. Li, *J. Phys. Chem. Lett.*, 2019, **10**, 6551–6557.
149 S. Cao, S. Wei, X. Wei, S. Zhou, H. Chen, Y. Hu, Z. Wang, S. Liu, W. Guo and X. Lu, *Small*, 2021, 2100949, DOI: 10.1002/smll.202100949.
150 Q. Yuan, Y. Li, P. Yu, B. Ma, L. Xu, Q. Sun, H. Yang, M. Xie and T. Cheng, *J. Exp. Nanosci.*, 2021, **16**, 256–265.
151 K. K. Rao, Q. K. Do, K. Pham, D. Maiti and L. C. Grabow, *Top. Catal.*, 2020, **63**, 728–741.
152 D. Gao, T. Liu, G. Wang and X. Bao, *ACS Energy Lett.*, 2021, **6**, 713–727.

153 Z.-K. Han, D. Sarker, R. Ouyang, A. Mazheika, Y. Gao and S. Levchenko, *Nat. Commun.*, 2021, **12**, 1–9.
154 X. Ma, Z. Li, L. E. Achenie and H. Xin, *J. Phys. Chem. Lett.*, 2015, **6**, 3528–3533.
155 Z. W. Ulissi, M. T. Tang, J. Xiao, X. Liu, D. A. Torelli, M. Karamad, K. Cummins, C. Hahn, N. S. Lewis and T. F. Jaramillo, *ACS Catal.*, 2017, **7**, 6600–6608.
156 J. R. Kitchin, *Nat. Catal.*, 2018, **1**, 230–232.
157 Y. Chen, Y. Huang, T. Cheng and W. A. Goddard III, *J. Am. Chem. Soc.*, 2019, **141**, 11651–11657.
158 K. Tran and Z. W. Ulissi, *Nat. Catal.*, 2018, **1**, 696–703.
159 M. Zhong, K. Tran, Y. Min, C. Wang, Z. Wang, C.-T. Dinh, P. De Luna, Z. Yu, A. S. Rasouli and P. Brodersen, *Nature*, 2020, **581**, 178–183.
160 A. Chen, X. Zhang, L. Chen, S. Yao and Z. Zhou, *J. Phys. Chem. C*, 2020, **124**, 22471–22478.
161 X. Wan, Z. Zhang, H. Niu, Y. Yin, C. Kuai, J. Wang, C. Shao and Y. Guo, *J. Phys. Chem. Lett.*, 2021, **12**, 6111–6118.
162 X. Wan, Z. Zhang, W. Yu and Y. Guo, *Materials Reports: Energy*, 2021, **1**, 100046.
163 T. Zheng, K. Jiang, N. Ta, Y. Hu, J. Zeng, J. Liu and H. Wang, *Joule*, 2019, **3**, 265–278.
164 M. G. Kibria, J. P. Edwards, C. M. Gabardo, C. T. Dinh, A. Seifitokaldani, D. Sinton and E. H. J. A. M. Sargent, *Adv. Mater.*, 2019, **31**, 1807166.
165 T. Cheng, H. Xiao and W. A. Goddard III, *J. Am. Chem. Soc.*, 2016, **138**, 13802–13805.

